Stony Brook University

EXPERIMENTAL CONSTRAINT ON HYDROMECHANICAL PROPERTIES AND MICROCRACK FABRIC OF CORE SAMPLES FROM THE TAIWAN CHELUNGPU-FAULT DRILLING PROJECT

A Thesis Presented

by

Tzu-Mo Chen

to

The Graduate School

in Partial Fulfillment of the

Requirements

for the Degree of

Master of Science

in

Geosciences

Stony Brook University

May 2008

Stony Brook University

The Graduate School

Tzu-Mo Chen

We, the thesis committee for the above candidate for the Master of Science degree, hereby recommend acceptance of the thesis.

Teng-fong Wong, Thesis Advisor
Professor, Department of Geosciences, Stony Brook University

Daniel M. Davis, Chairperson of Defense
Professor, Department of Geosciences, Stony Brook University

Wenlu Zhu
Assistant Professor, Department of Geology, University of Maryland

This thesis is accepted by the Graduate School.

Lawrence Martin
Dean of the Graduate School

Abstract of the Thesis

EXPERIMENTAL CONSTRAINT ON HYDROMECHANICAL PROPERTIES AND MICROCRACK FABRIC OF CORE SAMPLES FROM THE TAIWAN CHELUNGPU-FAULT DRILLING PROJECT

by

Tzu-Mo Chen

Master of Science

in

Geosciences

Stony Brook University

2008

Hydromechanical properties of core samples that were retrieved from the Taiwan Chelungpu Drilling Project (TCDP) borehole-A have been investigated in the laboratory. Cylindrical samples were cored in the mutually perpendicular directions to determine the anisotropic behavior. Conventional triaxial compression tests were performed at room temperature to determine the brittle strengths of intact samples and residual friction strengths of the fractured samples. Nominally dry samples were deformed under 20 MPa confining pressure, and samples saturated with distilled water were deformed under 30, 50 and 70 MPa confining pressures and 10 MPa pore pressure. The permeabilities of samples saturated with distilled water were measured by either steady state or pulse transient technique. A series of microscopic observation were performed to characterize

the microstructure that controls the anisotropy behavior in the samples.

The shaly siltstone samples show significant water weakening. The presence of water resulted in ~32 % reduction in the strengths of the saturated samples relative to the corresponding dry samples cored in the same direction. The high clay content would make the siltstones mechanically weak, and the strengths of these siltstones are actually comparable to the sandstones with higher porosities. The frictional coefficients of fractured samples were determined to range from 0.68 to 0.87 under wet condition. The mechanical behaviors are influenced by the bedding anisotropy. The stiffness and brittle strength of samples cored vertically were somewhat lower than those of the horizontal samples. The failure mode in the siltstone samples which were cored perpendicular to the strike of the core axis and bedding implies that bedding anisotropy may have dominant control over the style of faulting.

The sandstones are more permeable than the shaly siltstones, with permeability values on the order of 10^{-14} to 10^{-17} m^2. The shaly siltstones are much tighter, with permeabilities on the order of 10^{-16} to 10^{-19} m^2. Similar with mechanical strength, the permeabilites of shaly samples were also controlled by the bedding. Our laboratory data on the shaly siltstone samples indicate that thermal pressurization of pore fluid would be expected in the TCDP shaly rocks and may provide a mechanism of dynamic weakening of Chelungpu fault.

More than ninety thousand observable microcracks data in three sandstone samples were analyzed and the resulting crack tensor is found to agree well with the orientation of the principal P-wave velocity axes at these depths. The preferential microcrack planes are subparallel to the direction of the tectonic maximum principal stress.

Table of Contents

List of Figures

List of Tables

Acknowledgements

First, I would like to thank my advisor Teng-fong Wong for leading me into the interesting world of rock mechanics. I learned the professional knowledge and laboratory skill, as well as the ways of thinking and the proper attitude of doing research in the academia. I am also grateful to Wenlu Zhu for giving me tremendous help in experimental work and discussion. Professor Sheng-Rong Song in National Taiwan University, who is the PI of the Taiwan Chelungpu-fault Drilling Project, provided great support to this project, mentally and financially. My committee member, Dan Davis provided important comments and valuable suggestions both to the project and the writing of this thesis.

I also thank lab mates at Stony Brook University, including Wei Zhu and Sheryl Tembe, for their unceasing encouragement during my study. Special thanks to Veronika Vadjova, who spent a lot of time and showed great patience to teach me how to operate the machine. Laurent Louis kindly shared his experience with me and guided me through part of this project.

In the end, I am most appreciative to my parents, sisters and my husband for their doubtless and unconditional support of my life and research work. Their support gives me strength to finish this task. I really thank my husband for his consideration during this time period and his suggestions and valuable inputs on the project and the thesis presentation.

Publications

Louis, L., **T.-M. N. Chen**, C. David, P. Robion, T.-f. Wong and S.-R. Song (2008), Anisotropy of magnetic susceptibility and P-wave velocity in core samples from the Taiwan Chelungpu-fault Drilling Project (TCDP), *Journal of Structural Geology*, in press, SG-D-07-00157R1.

Chen, T.-M. N., W. Zhu, T.-f. Wong and S.-R. Song (2008), Laboratory characterization of permeability and its anisotropy of Chelungpu fault rocks, *Pure And Applied Geophysics*, submitted.

CHAPTER 1

INTRODUCTION

1.1 Tectonic Setting

Earthquakes that happen at active plate margins often cause great damage and many casualties. Taiwan is located at the plate boundary of the Eurasian continental plate and the Philippine Sea Plate (Figure 1.1), and the plate motion makes Taiwan seismically active. Near the northeast coast of Taiwan, the Philippine Sea Plate is subducted under the Eurasian Plate and causes high seismicity along a north-dipping seismic zone. The Eurasian oceanic lithosphere of South China Sea Plate is subducted eastward beneath the lithosphere of Philippine Sea Plate around the south coast of Taiwan, taking shape of an east-dipping seismic zone. The average rate of the oblique convergence of these two plates could be as fast as 80 mm per year. The plate collision induced folding and thrust faulting on the island of Taiwan, especially in the middle region of western Taiwan where a large population resides. Historically, at least 6 earthquakes with magnitudes M_L larger than 7 occurred in Taiwan during the twentieth century and resulted in severe damage (*Shin and Teng*, 2001). This strong and active orogeny has lasted few million years and is still in progress (*Ho*, 1986; *Teng*, 1987, 1990, 1996).

1.2 1999 Chi-Chi Earthquake

The M_w 7.6 Chi-Chi earthquake that took place on September 21, 1999 (local time) was induced by movement of the Chelungpu thrust fault at a focal depth of 10 km (*Kao and Chen*, 2000). With the epicenter at 120.82°E and 23.85°N, the earthquake produced a

roughly 90-km-long surface break in the north-south direction and a 20-km-long west-east extension in the northern tip (Figure 1.2) in central Taiwan. Studies of paleoseismology based on radiocarbon dates and historical earthquake records indicate that the timing of the Chelungpu fault's penultimate movement was between 430 and 150 years ago, and the average recurrence interval of the movement is less than 700 years (*Chen et al.*, 2004). The rupture during this event initiated at the southern part of the Chelungpu fault according to the local seismic data, leveling and geological ground observation of the surface rupture (*Shin and Teng*, 2001). The recorded displacement and ground motion data showed quite different earthquake characteristics between the northern and southern portions of the rupture zone. In the northern part, the displacement was larger (up to 12 m) and slip motion was smoother with smaller high-frequency (>1 Hz) acceleration (~0.5 *g*) and higher ground velocity, and the damage is relatively low. In contrast, smaller displacement and large ground acceleration (larger than 1 *g*) were observed in the southern part (*Shin and Teng*, 2001; *Ma et al.*, 2003) (Figure 1.3a). These different behaviors may have resulted from involvements of various types of dynamic weakening mechanisms during the earthquake.

Several models of the fault geometry were derived from the spatial distribution of coseismic slip and slip velocity which were analyzed from the strong ground motion data, teleseismic data, and GPS displacement data that were collected by the Taiwan Strong Motion Network (TSMN) (~600 stations) and Global Positioning System (GPS) (~130 stations). The geometry of Chelungpu fault can be identified as a ramp-décollement structure with shallower detachment based on the coseismic GPS displacements (Figure 1.3b) (*Johnson and Segall*, 2004), the combination of the focal depth, focal mechanism, subsurface geology (*Kao and Chen*, 2000), and coseismic displacements with new 3D

map (*Yue et al.*, 2005). The Chelungpu fault is located within and dips 30° to the east parallel to the strike of the bedding of the Chinshui Shale Formation (Figure 1.4). In such geological environment, the deformation of materials occurs within the accretionary wedge above the basal décollement (*Davis et al.*, 1983). This internal deformation has induced the anisotropy of physical properties and represents the mechanical model in the upper crust. Fluid overpressurization near the décollement, which is a more impermeable layer, and within the wedge could cause the weakening of material and localization of faulting (*Suppe and Wittke*, 1977).

1.3 Taiwan Chelungpu-fault Drilling Project (TCDP)

Taiwan Chelungpu-fault Drilling Project (TCDP) is an international cooperative project that started after the Chi-Chi Earthquake took place in 1999. The objective of this project is to investigate the physical and chemical properties that control the faulting mechanisms during the seismic cycle to understand the dynamic faulting process. The northern portion of the Chelungpu fault where larger displacement occurred during Chi-Chi earthquake was selected to be the drilling site. In Takeng, Taichung, two vertical boreholes (Hole-A and -B) just 45 m away from each other and one side-track (Hole-C) from Hole-B at the depth of 950 to1280 m were drilled between the years of 2004 to 2006. Cuttings were collected in the upper 431.34 m, and continuously coring and geophysical logging were also completed at the depth of 431.34 to 2003.26 m in Hole-A and from 950 to 1352.6 m in Hole-B. The recovery of the core samples was over 97%.

Hole-A penetrated three formation units, Cholan (0 to 1029 m), Chinshui (1029 to 1303 m) and Kueichulin (1303 to 1712 m) formation with the age from the youngest to

the oldest (*Song et al.*, 2007) (Figure 1.4). The Cholan formation (1712-2003 m) appeared again beneath the Kueichulin formation. The late Pliocene to the early Pleistocene Cholan formation is composed of sandstone, siltstone, shale, sandstone with silty intervals, shale with sandy intervals and siltstone with sandy intervals. The lithology of the late to the early Pliocene Chinshui formation is dark gray shale with sandy or silty intervals. Greenish-gray shaly sandstone, gray sandstone and shale are dominant in the late Miocene to the early Pliocene Kueichulin formation (*Ho*, 1988; *Song et al.*, 2007).

A well-developed fault zone architecture typically consists of fault core, damage zone, and protolith (*Sibson*, 1977; *Chester and Logan*, 1986; *Caine et al.*, 1996). The fault zone itself comprises two components: the fault core, where the most intense displacements occur and the associated damage zone which is characterized by extensive fractures and small faults. The protolith represents the relatively intact, undeformed country rocks. In TCDP Hole-A, several fault zones were identified with thick fault gouge at the depth of 1111, 1153, 1222, 1580, 1712 and 1812 m. Fault zone 1111 m (FZ1111) at depths ranging from 1106.29 to 1111.79 m is characterized by extensive fractures. It is considered to be the major slip zone associated with the 1999 Chi-Chi earthquake (*Song et al.*, 2007) based on these observations: the appearance of pseudotachylyte (*Kuo and Song*, 2005), decreased resistivity and permeability, lowest density, V_p and V_s, high V_p/V_s, Poisson ratio and fluid contents (*Hung et al.*, 2007), and anomalously high CO_2, CH_4 gas content (*Yang et al.*, 2005). In the fault zone FZ1111, clay gouges of fault core appears at the depth of 1110.37-1111.34 m, surrounded by the asymmetric damage zone. Fault zone at the depth of 1712 m represents another major thrust fault – Sanyi fault, with drastic change of fast polarization direction (*Hung et al.*, 2007).

1.4 Dynamic Weakening Mechanism

Several hypotheses have been proposed to explain the dynamic weakening mechanisms that can take place in the fault system during the earthquake, including frictional melting, elastohydrodynamic lubrication, and thermal pressurization. Thermal pressurization of the pore fluid is induced by frictional heating. The pore pressure would increase due to the elevated temperature that was created by the friction in the slip zone. As a result, the effective pressure and frictional strength would be reduced (*Sibson*, 1973; *Lachenbruch*, 1980; *Mase and Smith*, 1987; *Lee and Delaney*, 1987). *Andrews* (2002) suggested that thermal pressurization dominates the stress drop process during dynamic rupture beyond a threshold distance. The threshold distance is proportional to the hydraulic diffusivity and inversely proportional to the square of the frictional coefficient. The hydraulic diffusivity is defined as

$$\omega = \frac{k}{\phi\eta\beta} = \frac{k}{\phi S_s} \tag{1}$$

where k is the permeability, ϕ is the porosity, η is the viscosity, β is the total compressibility ($\beta = \beta_f - \beta_s + (\beta_b - \beta_s)\phi$, where β_f, β_s and β_b denote the fluid, solid and bulk compressibilities, respectively), and S_s is the storage capacity. The threshold distance estimated with friction coefficient of 0.7 and hydraulic diffusivity of 0.02 m^2/s based on measurement of fault core samples in laboratory and assuming the frictional coefficient comparable to Byerlee's Law is about 300 m. This distance is comparable to the fault dimension of an earthquake with the magnitude of 3.5. This result indicates that thermal pressurization would be dominant at rupture distances greater than 300 m. However, the hydraulic diffusivity derived from the permeability measured in the field is usually larger than that measured in the laboratory (*Brace*, 1980). Dilatancy and higher value of

permeability would reduce the effect of thermal pressurization. If the value of the hydraulic diffusivity is two orders of magnitude larger than the laboratory-derived value, the thermal pressurization would be effective in large earthquake events.

1.5 Anisotropy of Physical Properties

Anisotropy of some physical properties is associated with the fabric and structure, such as bedding, preferential arrangement of minerals and cracks, within the rocks. The texture of the rocks could result in the anisotropy of strength that may relate to the different failure modes and deformation mechanisms and spatial distribution permeability that could influence the transportation of fluid. Since the mechanical and hydraulic properties of the fault system constrain the rupture behavior, the investigation of anisotropy would be especially important. Studies of anisotropic properties could help interpret not only the fault mechanisms, but also the in situ tectonic stress field.

Previous studies have shown that appreciable anisotropy in mechanical behavior may result from planar rock fabric, cleavage, and preferential orientation and arrangement of minerals and cracks. In sedimentary rocks, bedding, foliation in the matrix and pore space anisotropy are the factors than can induce the anisotropy of physical properties. For metamorphic rocks such as gneiss, phyllite, schist and slate, the minimum brittle strengths were observed at intermediate bedding angles (*Donath*, 1972; *Nasseri et al.*, 1977; *Vernik et al.*, 1992), as well as shale (*Niandou et al.*, 1997). However, this phenomenon may not appear in all porous sandstones. For porous sandstones, the brittle strengths increased from the minimum to its maximum while the direction of the applied stress changes from parallel to the bedding to perpendicular to the bedding (*Baud*

at al., 2005). The experimental data of P-wave velocity, magnetic susceptibility, permeability and electrical conductivity implied that bedding and pore space may be considered as two different scenarios for the development of anisotropy.

1.6 Scope of This Study

The different rupture behavior between the northern and southern portions of the Chelungpu fault is a key attribute of the 1999 Chi-Chi earthquake. What are the deformation mechanisms within the fault zone? What are the mechanical properties of fault-related rocks with depth? What is the permeability evolution of fault rocks? What is the extent of the anisotropic behavior of the mechanical and permeability properties? What are the factors that control the anisotropic behavior within the rocks? To answer these questions, we conducted measurement of physical properties of this fault system to provide insights into the deformation mechanisms of such a large earthquake, and characterize the anisotropy behavior in relation to both matrix and pore space.

In this study, we have investigated the hydromechanical properties of the rock samples in the laboratory, such as the mechanical strength, frictional strength, and permeability, to help us determine the deformation mechanism during the earthquake and microstructure within the fault-related rocks, and to clarify how the internal texture controls the anisotropy of physical properties.

In Chapter 2, I will describe the materials retrieved from TCDP that were used to investigate the hydromechanical properties and anisotropy and how we chose the sampling locations. The experimental set-up and procedure for this study are introduced as well in this chapter.

Chapter 3 includes the results of the measurements and the discussions of the data. The results would reveal the characteristics of anisotropy in both siltstone and sandstone samples. The microstructural observations provide interpretation of the anisotropy properties. Moreover, I will try to apply the experimental data to constrain the feasibility of thermal pressurization during the Chi-Chi earthquake.

In the last chapter, I will conclude the observations in this study. Since the studied materials were limited, more measurements on samples at various depths are going to be conducted in the future to provide more complete insight into the rupture mechanics of the Chelungpu fault.

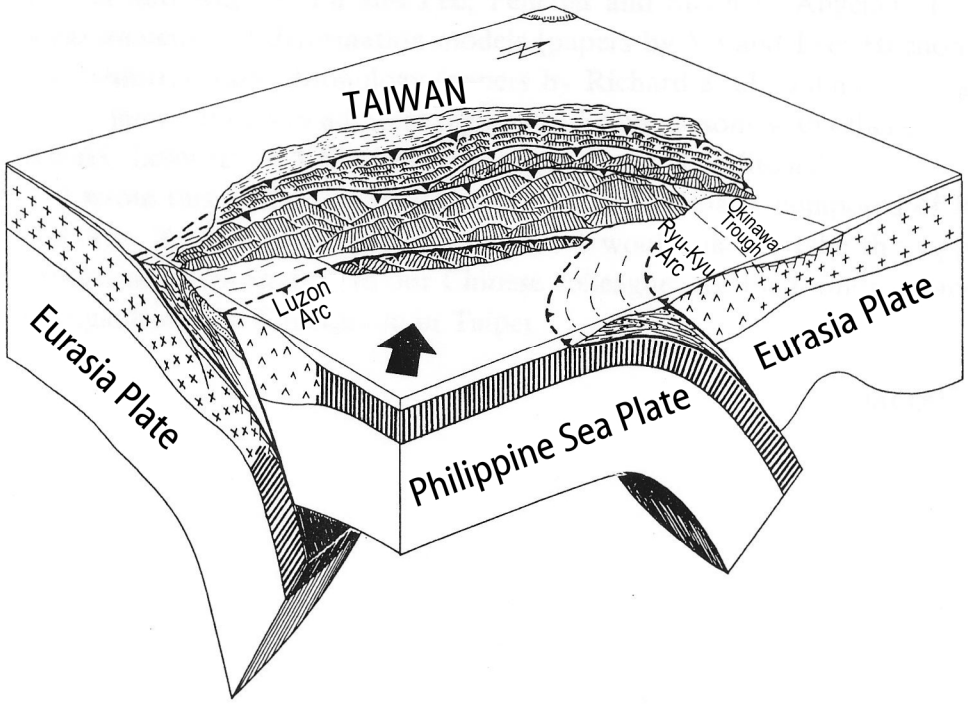

Figure 1.1 Tectonic setting of the Taiwan region (*Angelier*, 1986). Near the northeast of Taiwan, the Philippine Sea Plate is subducted under the Eurasia Plate. Around the south of Taiwan, the Eurasian oceanic lithosphere of the South China Sea Plate is subducted eastward beneath the lithosphere of the Philippine Sea Plate. The convergence rate is ~80 mm per year.

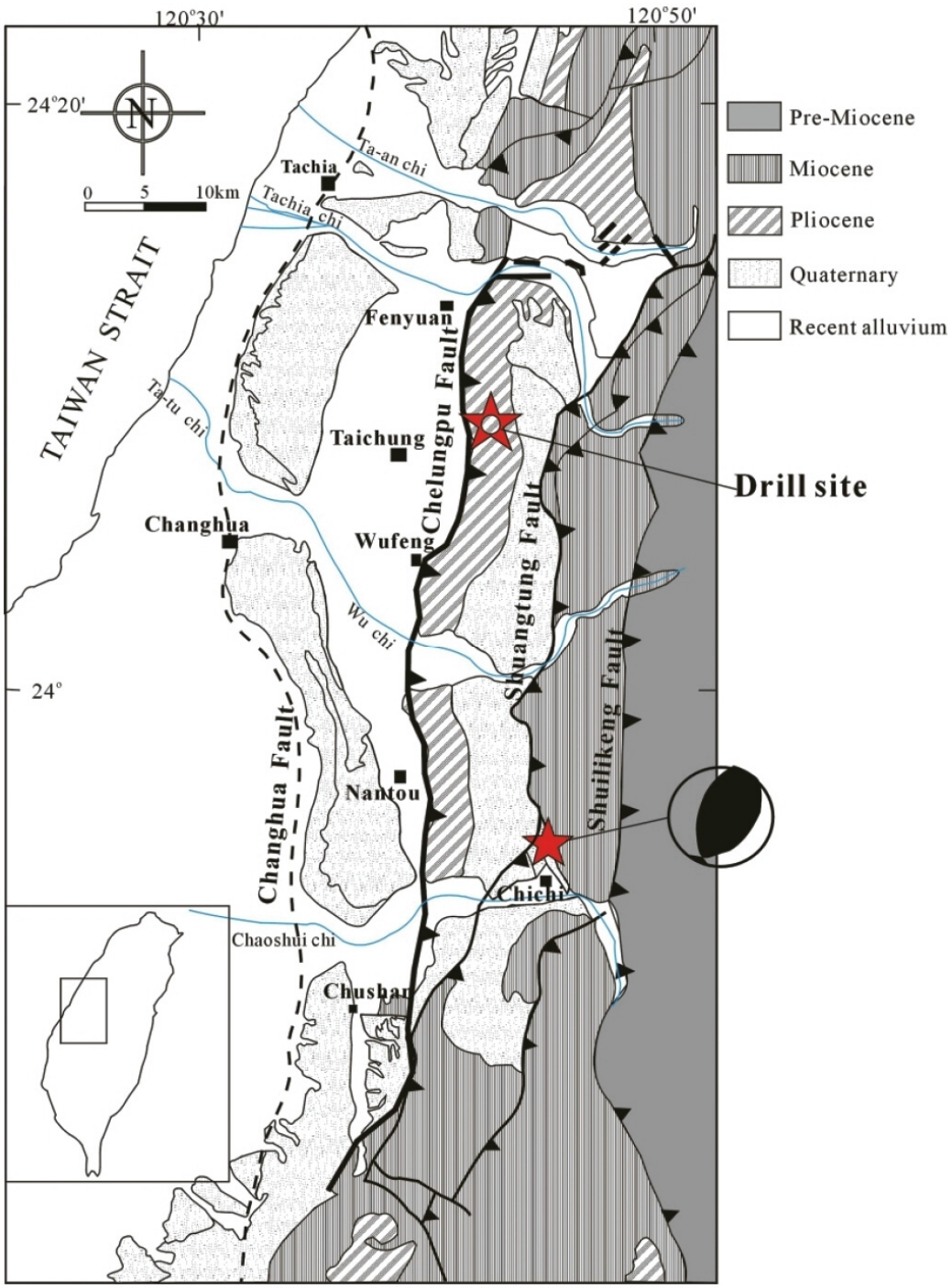

Figure 1.2 Geological map near the TCDP drill site in Takeng, Taichung, showing the surface rupture of the Chelungpu fault and the focal mechanism of the 1999 event. The red star connected to the focal mechanism denotes the epicenter of this event which is near Chi-Chi (*Song et al.*, 2007).

a)

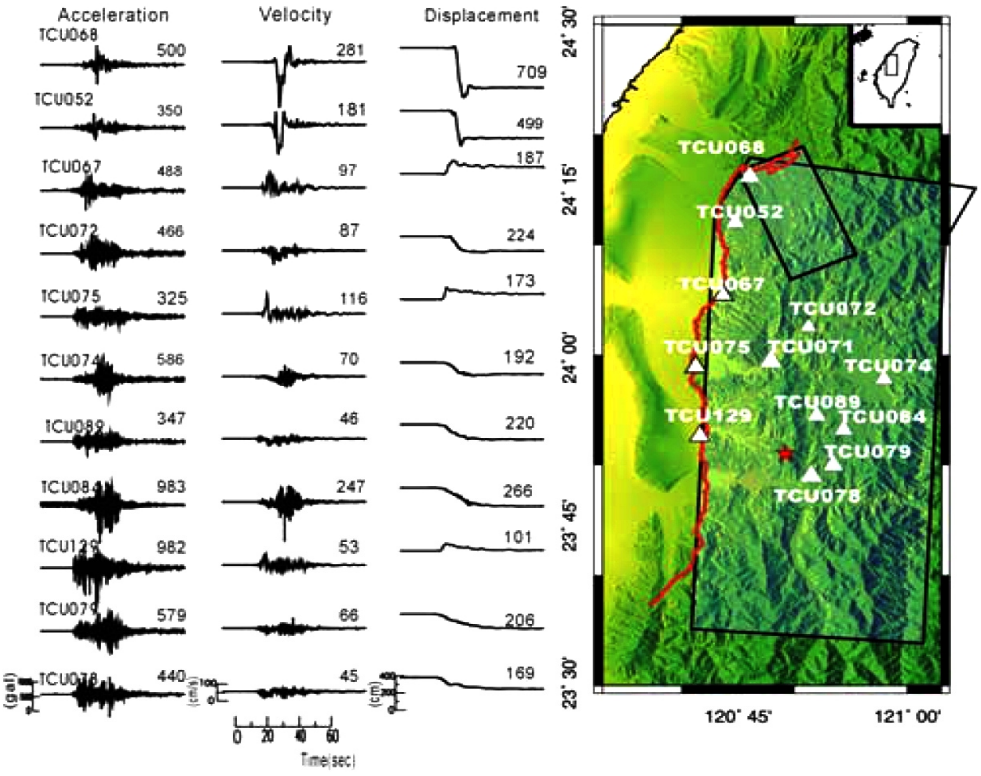

Figure 1.3a The east-west component of acceleration, velocity and displacement seismograms for the near-field strong-motion stations (triangles) along the fault rupture (red solid line) and on the hanging wall during the Chi-Chi earthquake. The unit for the acceleration, velocity and displacement on each seismogram are in gal, cm/s and cm, respectively (*Ma et al.*, 2003).

b)

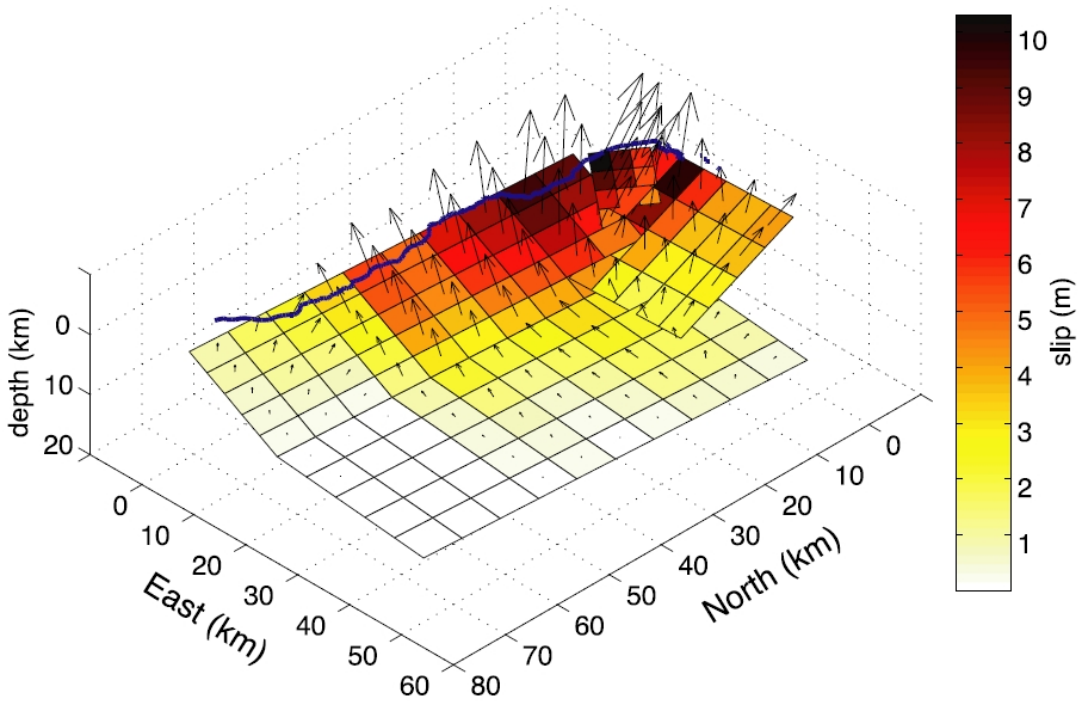

Figure 1.3b Slip distribution for the fault geometry model inferred from inversion of geodetic data (*Johnson and Segall*, 2004). The maximum displacement occurred near the join between the main north-south surface break and the west-east extension in the northern tip of the Chelungpu fault. This three-fault model shows that the Chelungpu-fault is a ramp-décollement structure with shallower detachment.

a)

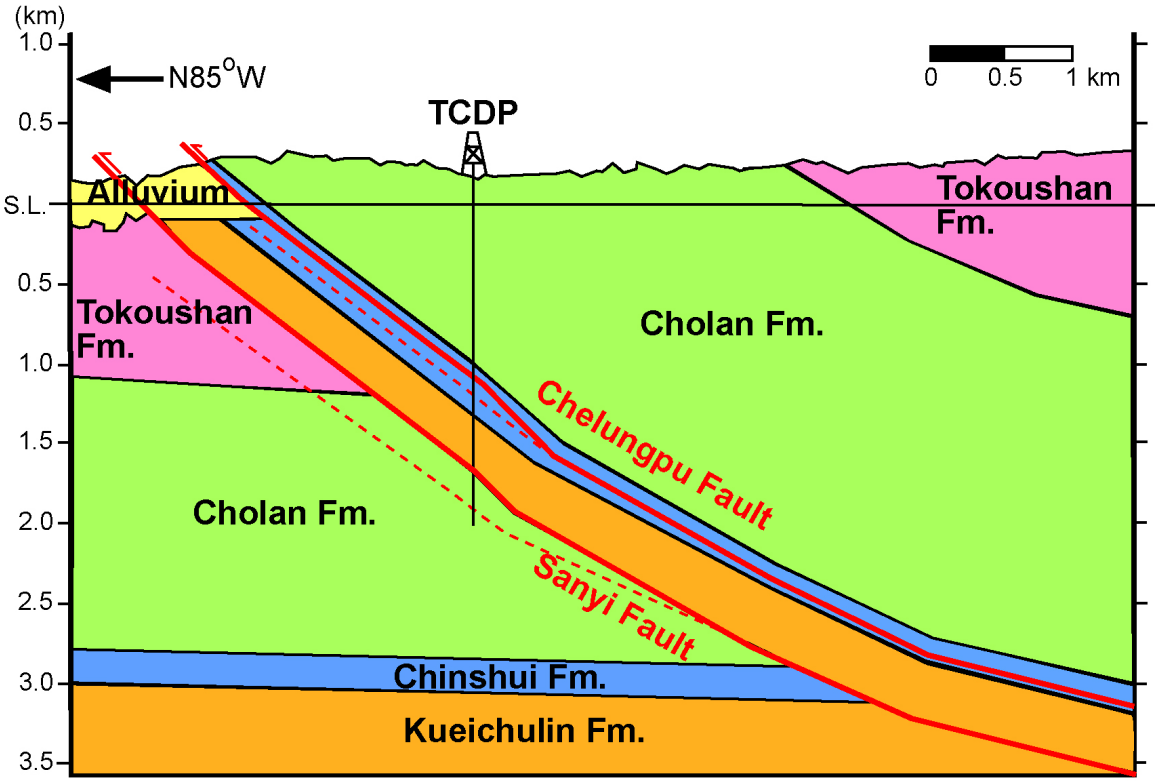

Figure 1.4a Schematic cross section near the TCDP drill site (modified from *Yeh et al.*, 2007; *Hung et al.*, 2007), showing the formation distribution and major faults. The borehole encountered the Chelungpu fault within the Chinshui formation and the Sanyi fault near the contact of the Kueichulin and Cholan formations.

b)

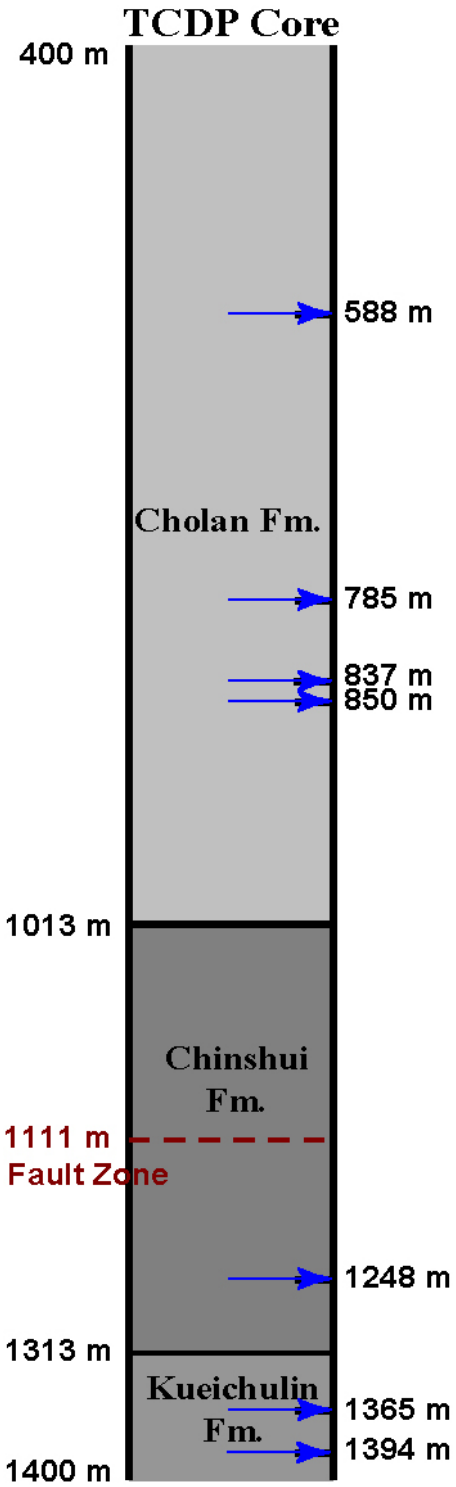

Figure 1.4b Stratigraphic column in TCDP Hole-A. The fault zone which is associated with Chi-Chi earthquake is identified by red dashed line. Blue arrows indicate the sampling locations.

CHAPTER 2

TCDP SAMPLE DESCRIPTION AND EXPERIMENTAL PROCEDURE

2.1 Sample Description and Preparation

Due to the limited quantity of samples from the fault zone and the requirement of larger-sized samples needed for the mechanical and permeability tests, our experiments were done only on selected country rocks retrieved from TCDP Hole-A. Sampling locations were decided referring to the core description, logging data, and mud gas analysis. Intact samples without macroscopic fractures were preferred. Based on the logging data and gas analysis, locations with lower V_p and V_s, anomalously high CH_4, CO_2, and radon gas concentration (*Hung et al.*, 2007; *Yang et al.*, 2005) were selected to sample. The samples were collected from various depths above and below the major slip zone of Chelungpu fault.

The lithological facies in the borehole are dominantly siltstone (Figure 2.1a), sandstone (Figure 2.1b), and shale. The relatively tight siltstones are composed of quartz, more than 20 % clay minerals, and minor feldspar. These shaly siltstones have porosities of about 4 to 6 % and densities of ~2600 kg/m^3. The bedding identified by the lamination of clay minerals is dipping by about 30° to the east. Porous sandstones are predominated by quartz with minor feldspar. The porosities of sandstones range from 15 to 18%, and the densities are ~ 2100 kg/m^3. Both siltstone and sandstone samples at depths from 588 to 1248 m in Hole-A were investigated in this study (Table 2.1 and Figure 1.4b).

To investigate the anisotropy of mechanical and hydraulic transport properties, cylindrical samples were grounded along three orthogonal directions (direction X, Y and Z in Figure 2.2a) for each rock core retrieved from the TCDP borehole-A with various

distributions of bedding inside the samples (Figure 2.2b). Direction Z is parallel to the TCDP core axis, and the other two directions are perpendicular to the core axis, with X (N105°E) perpendicular and Y (N15°E) parallel to the strike of the bedding. The dimensions of our samples used for our measurement is 18.4 mm in diameter and 38.1 mm in length.

Each sample was dried in vacuum at temperature of 80℃ for at least 24 hours and jacketed with thin copper foil. Steel end-plugs were placed at the two ends of the sample, and then three layers of heat-shrinkable polyolefine tubing were used to keep the rocks insulated from the confining pressure medium (kerosene). Electric resistance strain gages (TML type FLA 10-11, Tokyo Sokki Kenkyujo Co.) were attached to the surface of the copper foil to measure the axial and transverse strains of the dry samples.

Preliminary brine tests showed that these shaly siltstones would split when they were immersed in fluids including distilled water, tap water, and also 0.01, 0.02 and 0.05 M KCl solutions. It was likely that the clay minerals interacted with the solution and reduced the cohesion between the mineral grains. To prevent the samples from falling apart due to the presence of distilled water at the start of drained experiments, we first applied a confining pressure of 15 MPa to the dried samples, and then we evacuated the pore space and saturated the samples with distilled water at a pore pressure of 10 MPa. It took at least 36 hours to achieve complete saturation.

2.2 Mechanical Experiment

The measurement of mechanical strengths, frictional coefficient, and residual frictional strength of the TCDP samples (Table 2.2) under both dry and wet conditions

were performed in the conventional triaxial compression configuration (Figure 2.3a) with axial stress $\sigma_1 > \sigma_2 = \sigma_3$ at room temperature (Figure 2.3b and c). In the triaxial experiments for dry samples, the confining pressure ($P_c = \sigma_2 = \sigma_3$) was set at 20 MPa, which is comparable with the in-situ hydrostatic pressure. In drained experiments, pore pressure P_p was set constantly at 10 MPa and the confining pressures varied from 30, 50, to 70 MPa, therefore the corresponding effective pressures ($P_{eff} = P_c - P_p$) were 20, 40 and 60 MPa, respectively. The experiments were conducted at a nominal axial strain rate of 2×10^{-5} per second, which was sufficiently slow to ensure a fully drained condition.

The confining pressure with an accuracy of 0.1 MPa was kept as a constant with fluctuation within 1% during triaxial loading. The axial stress was measured with an external loading cell with an accuracy of 0.1 kN. The axial displacement was measured with the displacement transducer (DCDT) mounted outside the pressure vessel, and the displacement rate was servo-controlled at a constant strain rate. The volumetric strain for the dry sample was measured by two strain gages following the relation $\varepsilon_v = \varepsilon_{\parallel} + 2\varepsilon_{\perp}$, where $\varepsilon_{\parallel}$ and $\varepsilon_{\perp}$ are the axial and the transverse strains, respectively. The porosity change of water-saturated sample was derived from the pore volume change measured by a porosimeter with an uncertainty of 0.1 %.

After a shear fracture had developed in an initially intact sample, friction tests were conducted on the fractured sample. Such a fractured sample was loaded until friction sliding occurred, and the shear strength was measured. The coefficient of friction μ was determined from the ratio of the resolved shear stresses (τ) and normal stresses (σ_n):

$$\sigma_n = \frac{1}{2}(\sigma_1 + \sigma_3) + \frac{1}{2}(\sigma_1 - \sigma_3)\cos 2\theta \tag{2}$$

$$\tau = \frac{1}{2}(\sigma_1 - \sigma_3)\sin 2\theta \tag{3}$$

when θ is the angle between the axial direction and the normal to the fault plane.

2.3 Permeability Experiment

In this study, two different techniques were implemented to measure the permeability depending on the value of permeability of interest. The steady-state flow technique was applied to rocks with relatively high permeability ($k > 10^{-15}$ m^2), and pulse transient technique was used when the samples were more impermeable ($k < 10^{-15}$ m^2) (*Brace et al.*, 1968; *Bernabe*, 1987).

The principle of steady-state flow method is that the flowing fluid would adhere to the Darcy's law under steady-state conditions. When a constant pore pressure gradient is applied across the sample, the volumetric flow rate (V_w / t) through the sample should be proportional to the cross-sectional area of the sample (A), and the pore pressure difference between two ends of the sample (ΔP_p), and inversely proportional to the length of the sample (L). The permeability k is calculated from the equation (*Bernabe*, 1987)

$$\frac{V_w}{t} = k\frac{A\Delta P_p}{\eta L} \tag{4}$$

If the permeabilities are too low to achieve steady-state flow, the pulse transient technique is then applied. At the beginning of a measurement, the pore pressure is in equilibrium at 10 MPa in the whole system, and then the pore pressure at one end of the sample was suddenly perturbed by a small amount ΔP_p (< 1 MPa). To monitor the transient decay of this perturbation, a differential pore pressure transducer measured the difference between the upstream and downstream pore pressure. The differential pore pressure decays exponentially as a function of time (Figure 2.4), and the permeability k could be derived from the slope of this semi-logarithmic plot according to the equation

(*Brace et al.*, 1968)

$$\alpha = \left(\frac{kA}{\eta \beta_f L} \right) \left(\frac{1}{V_{up}} + \frac{1}{V_{dn}} \right) \tag{5}$$

where β_f is the compressibility of fluid, V_{up} and V_{dn} are volumes of the upstream and downstream reservoirs, respectively. Both positive and negative sign of the pore pressure pulse generated would be applied.

In this study, in situ permeabilities of both sandstone and siltstone samples (Table 2.3) were obtained by measuring the hydraulic flow along the axial direction at different loading stages during hydrostatic compaction and triaxial compression. At a given stress state, the pore pressure would take several hours to reach equilibrium. These two different techniques are applicable to the permeameter setting for operation in a triaxial system (Figure 2.5) in our laboratory (*Zhu and Wong*, 1997). We can switch from one to the other technique if necessary during an experiment. The compressive storage of the reservoirs are defined as the volume change per unit pressure change associated with upstream ($C_{up} = \Delta V_{up} / \Delta P_p = V_{up} \beta_f$) and downstream ($C_{dn} = \Delta V_{dn} / \Delta P_p = V_{dn} \beta_f$) reservoirs. In our setup, the storage C_{up} of the upstream reservoir is 3.18×10^{-8} m^3/MPa, and C_{up} is assumed to be infinite because the downstream reservoir is connected to a highly compressible accumulator.

2.4 Microstructural Observations

Physical properties such as mechanical strength, permeability, and seismic properties are strongly controlled by the mineral assemblage and the arrangement of grains, pores and microcracks (*Lo et al.*, 1986; *Louis et al.*, 2005). The measurement of anisotropy of

magnetic susceptibility and P-wave velocity of TCDP cores that were performed by *Louis et al.* (2007) have indicated that the elastic fabrics are quite different in two lithologic facies. The anisotropy of the P-wave velocity of the TCDP siltstone samples is controlled by the preferentially oriented matrix minerals, while that of the sandstone samples might be affected by the microcrack porosity. To quantitatively characterize the microcrack density and anisotropy, microscopic observations were conducted to investigate the petrofabric and microstructure within the TCDP sandstones that were selected from samples that *Louis et al.* (2007) used for magnetic and sonic measurements.

A total of 14 petrographic thin sections of the TCDP core samples were prepared. 2 thin sections of sandstone (T588 and T850) and 3 thin sections of siltstone (T785, T837 and T1248) samples were made without any regards to the orientation, focusing only on the mineral compositions and pore distributions. The other 9 thin sections of the three sandstone samples (T850, T1365 and T1394) were used to quantitatively characterize microcrack density and anisotropy. Three orthogonal sections with basal plane perpendicular to the X, Y and Z directions, respectively for each sandstone sample were made. 20 images were taken under the optical microscope with reflected light at a magnification of 50×, covering a total area of 83.544 mm^2 for each thin section. The intragranular microcracks distributed pervasively in the sandstone samples were manually traced on the images. These traced microcracks were then binarized, and the distributions of the crack orientations and lengths were statistically analyzed by the ImageJ software (NIH freeware).

Stereological measurement of the linear intercept density, which corresponds to the numbers of intercepts between microcracks and a test array of parallel reference lines in different orientations normalized by the total lengths of reference lines in an array were

also performed. Totally 180 test arrays at angles from 0° to 180° with an increment of 1° with respect to the horizon on the images. In this study, a program written with the Scilab software (Inria freeware) to count the intercepts density of microcracks was applied (*Louis et al.*, 2007).

Table 2.1 Description of samples from TCDP Hole-A studied.

Set Name	Depth (m)	Lithological Formation	Rock Type
T588	587.86-588.76	Cholan	sandstone
T785	785.45-785.95	Cholan	siltstone
T837	837.25-837.75	Cholan	siltstone
T850	850.34-850.84	Cholan	sandstone
T1248	1248.80-1249.21	Chinshui	siltstone

Table 2.2 Compilation of mechanical experiments. Direction Z is parallel to the TCDP core axis, and the other two directions are perpendicular to the core axis, with X (N105°E) perpendicular and Y (N15°E) parallel to the strike of the bedding.

Sample Name	Depth & Orientation	Initial Porosity ϕ (%)	Density (kg/m^3)	Effective Pressure (MPa) P_c - P_p	Saturation	Type of Experiment
Siltstone						
TC#02	T837-Z	4.2	2600	20	Dry	Triaxial
TC#03	T837-X	4.2	2600	20	Dry	Triaxial
TC#04	T837-Z	4.1	2600	285	Dry	Hydrostatic
				20	Dry	Triaxial
TC#05	T837-X	3.9	2600	20	Wet	Triaxial and friction test
TC#06	T837-Z	3.8	2600	250	Dry	Hydrostatic
				20	Wet	Triaxial and friction test
TC#13	T837-X	4.1	2600	40	Wet	Triaxial and friction test
TC#14	T837-Z	3.5	2600	40	Wet	Triaxial and friction test
TC#16	T837-Z	3.7	2600	60	Wet	Triaxial and friction test
TC#22	T1248-X	5.0	2600	20	Wet	Triaxial and friction test
Sandstone						
TC#09	T588-Z	18.7	2100	20	Wet	Triaxial and friction test
TC#10	T588-X	18.1	2100	20	Wet	Triaxial and friction test

Table 2.3 Compilation of permeability experiments.

Sample Name	Depth & Orientation	Initial Porosity ϕ (%)	Density (kg/m^3)	Effective Pressure (MPa) P_c - P_p	Experiment
Siltstone					
TC#07	T837-X	3.9	2600	40	Hydrostatic
TC#08	T837-Y	3.9	2600	40	Hydrostatic
TC#11	T837-Z	4.3	2600	40	Hydrostatic
TC#15	T837-Y	4.0	2600	20	Triaxial
TC#17	T837-X	4.3	2600	40	Hydrostatic
TC#18	T837-X	4.2	2600	40	Hydrostatic
TC#20	T1248-X	4.0	2600	40	Hydrostatic
TC#21	T785-X	6.7	2500	100	Hydrostatic
Sandstone					
TC#12	T588-Y	15.9	2200	20	Triaxial
TC#19	T850-X	18.6	2200	20	Triaxial

a)

b)

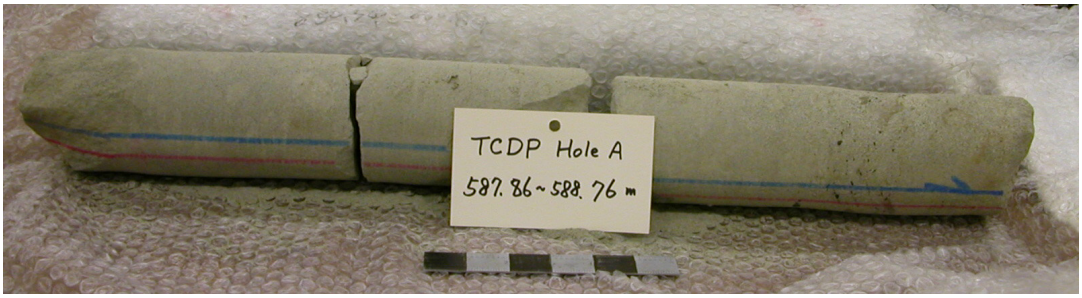

Figure 2.1 Photographs of TCDP core samples. The diameter of samples is ~80 mm. Red and blue lines are the reference of orientation. a) Shaly siltstone sample T837 with higher content of clay minerals was located at the depth 837.25 to 837.75 m. b) Bioturbated sandstone sample T588 with was located at the depth 587.86 to 588.76 m.

a)

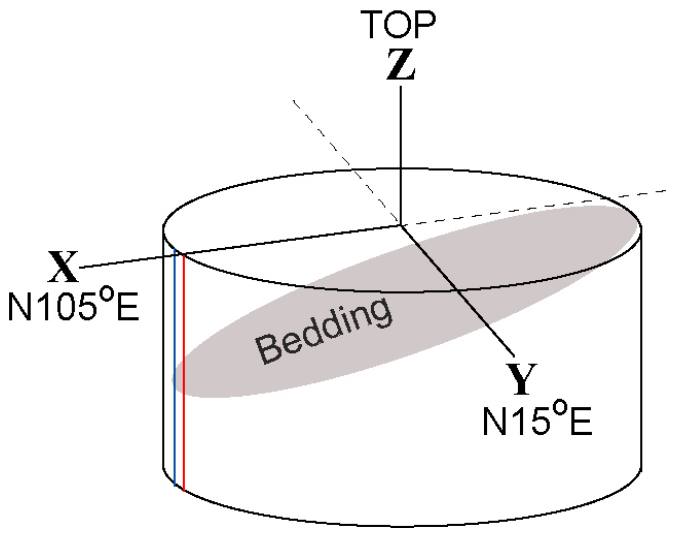

b)

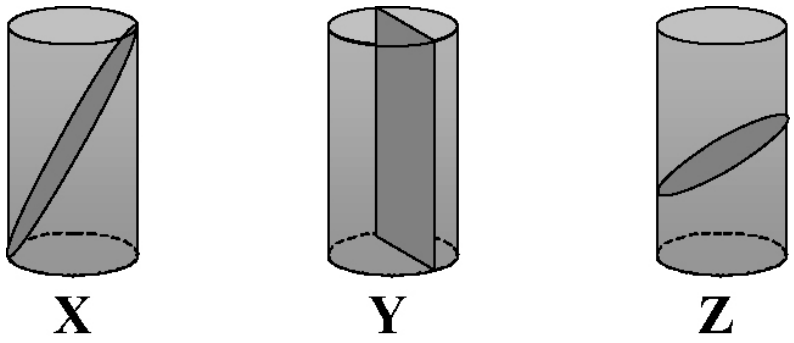

Figure 2.2 a) Sub-core sampling pattern. Cylindrical samples with the diameter of 1.8 mm and the length of 3.8 mm are cored along the direction X, Y and Z, respectively. b) Bedding orientation in cylindrical samples cored in three directions. The bedding is indicated by dark gray color. The angle between bedding and coring direction is 30°, 0°and 60° for sample X, Y and Z, respectively.

a)

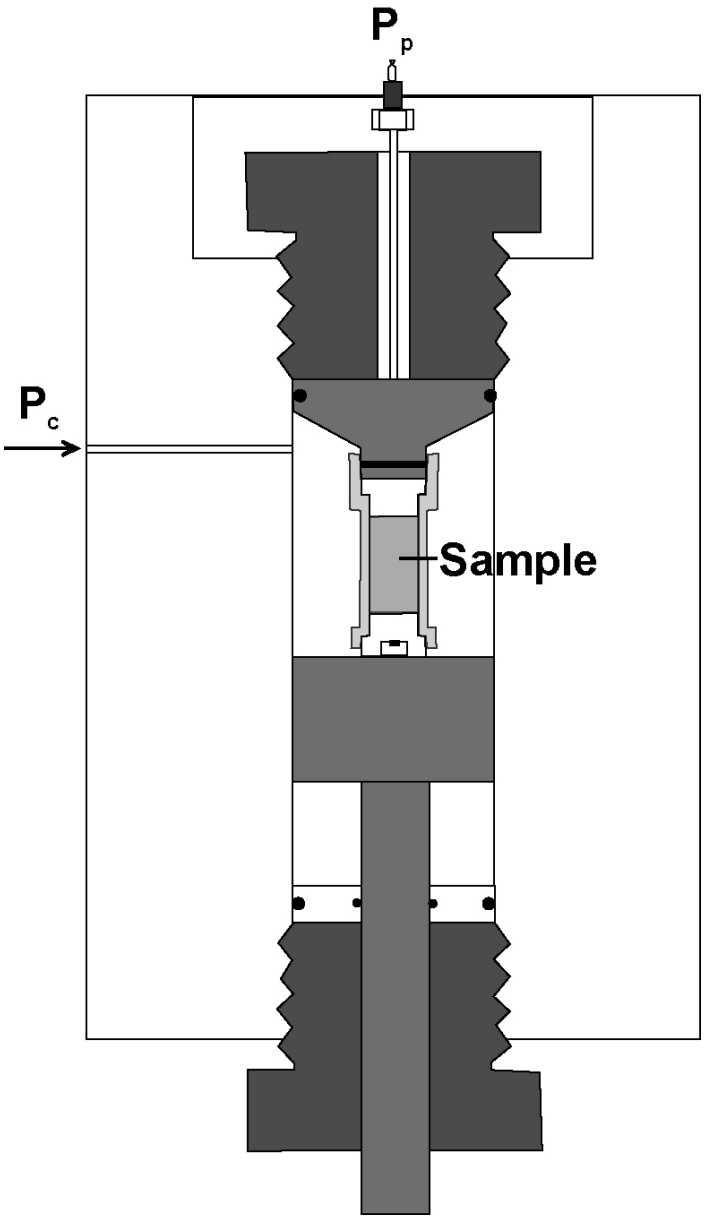

Figure 2.3 a) Experimental set-up for mechanical tests.

b) c)

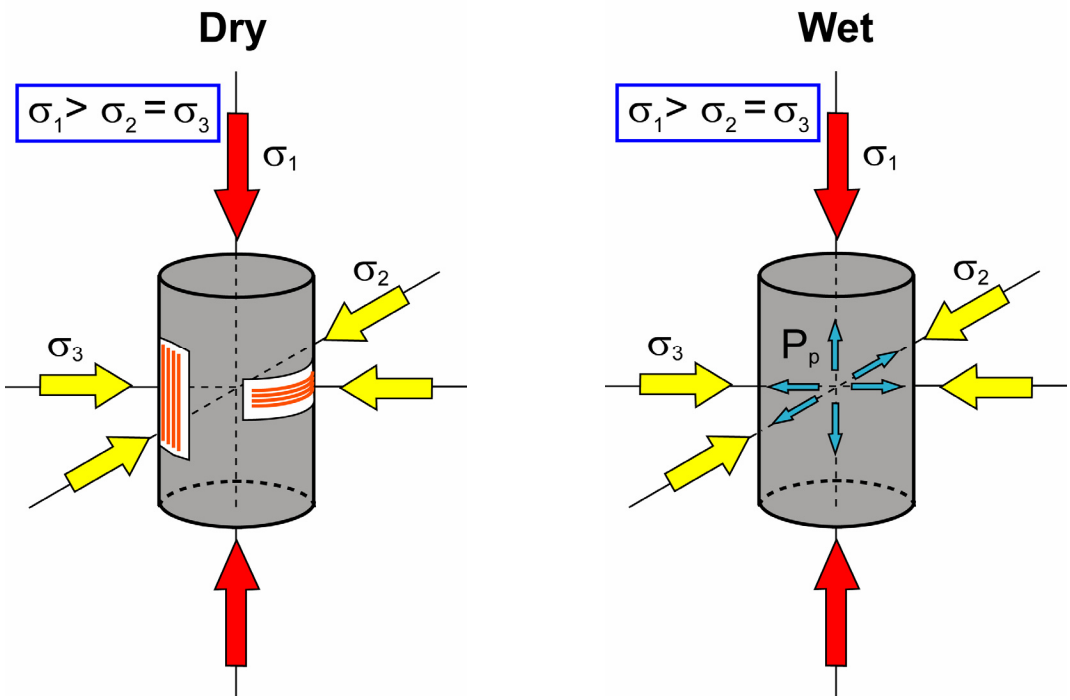

Figure 2.3 b) Stress state for dry samples. Maximum principal stress σ_1 is the axial stress, with intermediate and minimum principal stress σ_2 and σ_3 equal to the confining pressure P_c. Electric resistance strain gages were attached on the samples to measure the axial and transverse strains. c) Stress state for wet samples. Pore pressure P_p is calculated from the pore volume change which is measured by the porosimeter and kept constant at 10 MPa during the experiments.

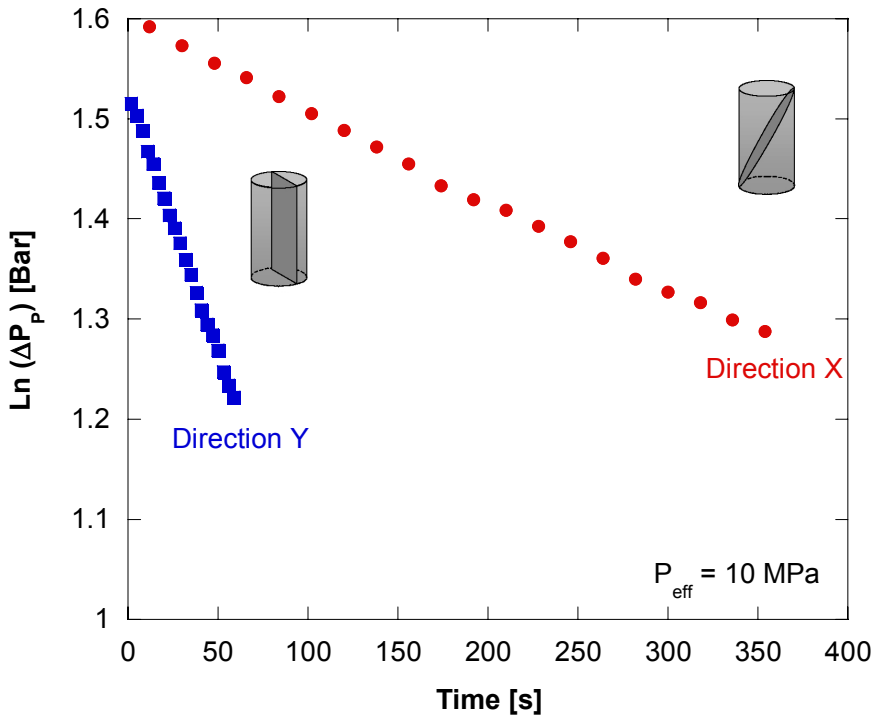

Figure 2.4 Differential pore pressure as a function of time in siltstone T837. The differential pore pressure decays exponentially with time. The permeability *k* could be derived from the slope of this semi-logarithmic plot (*Brace et al.*, 1968). The rapid decay of the sample cored in direction Y indicates that the samples cored along direction Y are more permeable than those cored in direction X.

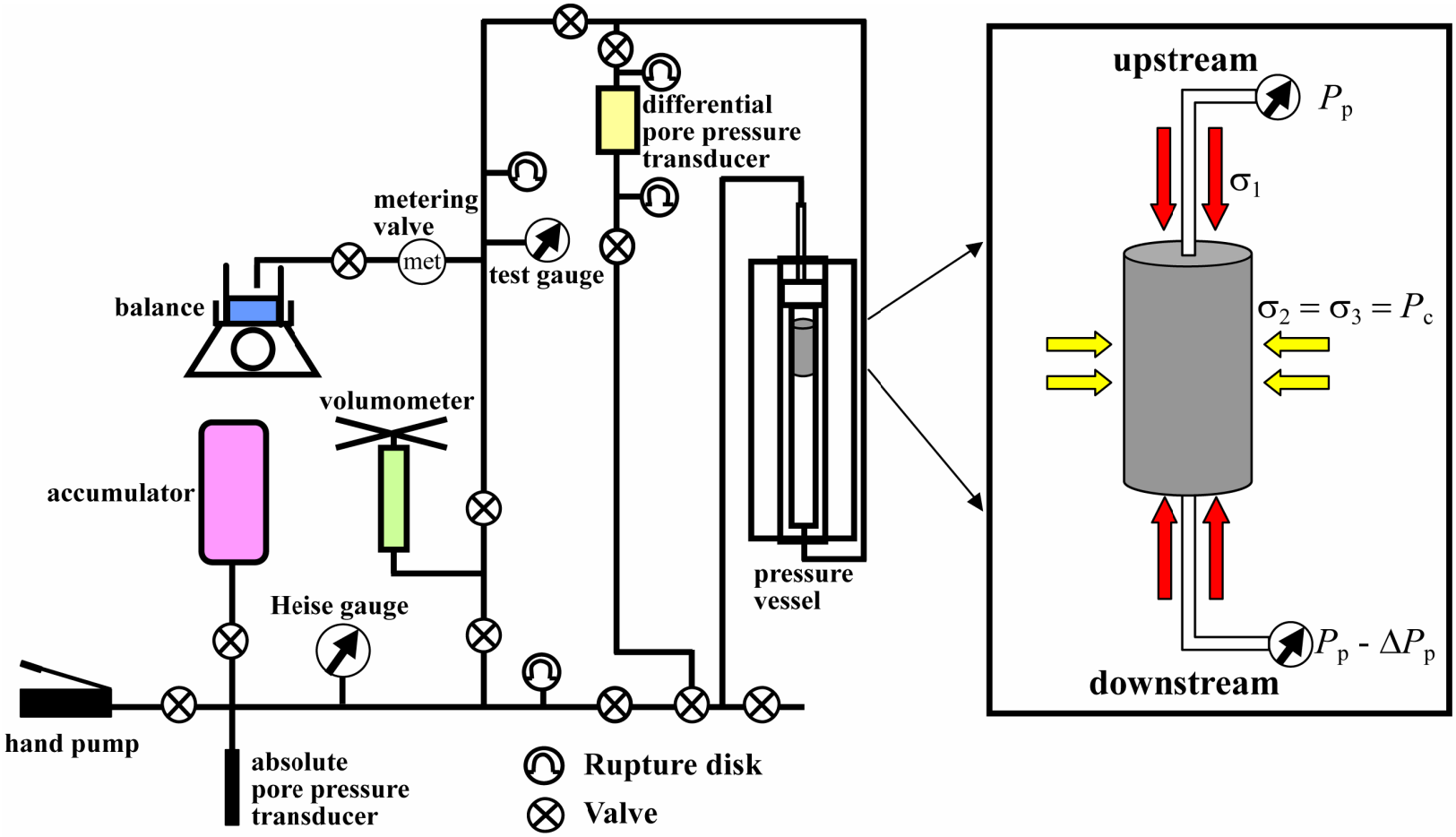

Figure 2.5 Experimental set-up for permeability measurements with stress state. The permeameter could perform by both steady state and pulse transient techniques. The permeability is obtained by measuring the hydraulic flow along the axial direction.

CHAPTER 3

RESULTS AND DISCUSSION

3.1 Mechanical Data

Mechanical deformation results were obtained from two shaly siltstone rocks (T837 and T1248) and one sandstone rock sample (T588) (Table 3.1). For each rock sample retrieved from different depths, cylindrical samples cored in direction X and Z (Figure 2.2a) were used to investigate the effects of bedding on the mechanical properties.

3.1.1 Mechanical Strengths

The mechanical data of sandstone T588 cored in direction X (TC#10) and Z (TC#09) that deformed at an effective pressure of 20 MPa under drained condition are shown in Figure 3.1a and b. The peak differential stress was 106 MPa for the sample cored in direction Z and 116 MPa for that cored in direction X (Figure 3.1a). The strengths of sandstone T588 are anisotropic, with the sample cored in direction X slightly stronger than that cored in direction Z. The porosity reduction as a function of axial strain is plotted in Figure 10b. The porosity initially reduced with axial strain until it reached C', defined as the onset of dilatancy prior to macroscopic fracture. After passing C' the porosity increased, possibly due to microcracking.

Dry siltstone samples were triaxially compressed at a confining pressure of 20 MPa, and water-saturated ones at confining pressures of 30, 50 and 70 MPa with a pore pressure of 10 MPa (corresponding to effective pressures of 20, 40 and 60 MPa, respectively). The mechanical strengths data of dry shaly siltstone samples deformed at

effective pressure of 20 MPa are plotted as a function of axial strain in Figure 3.2a. The differential stress increased with axial strain to reach a peak, followed by strain softening. The peak differential stresses ($\sigma_1 - \sigma_3$) of nominally dry samples (TC#02 and TC#03) at an effective pressure of 20 MPa are about 160 to 170 MPa and those of water-saturated ones (TC#05 and TC#06) are about 110 to 117 MPa regarding orientations of samples.

Our data show that brittle strengths of the wet siltstone samples were lower than the dry ones by about 30%, regardless of whether the samples were cored in either direction X or Z. The post-peak stress drops were also larger for dry samples than wet samples. With respect to the core orientation, strengths of samples cored in direction X (TC#03 and TC#05) are slightly stronger than those cored in direction Z (TC#02 and TC#06) under both dry and wet conditions. Similar to sandstone T588, the strengths of siltstone T837 are anisotropic, with the sample cored in direction X stronger than that cored in direction Z. Figure 3.2a shows that protolith T837 (TC#05) and T1248 (TC#22) located in the hanging wall and footwall of the Chelungpu fault, respectively, have comparable brittle strengths under the same saturation and effective pressure condition and coring orientation. Even though the porosities are significantly different for TCDP siltstones and sandstones, the mechanical strengths are quite comparable. Low porosity can increase the strength of shaly siltstones samples, but high content of clay minerals tend to make it weaker.

The volumetric strain (for dry siltstone samples) and porosity reduction (for saturated siltstone samples) are shown as functions of axial strain in Figure 3.2b. The volumetric strains and porosity reductions would decrease with increasing axial strains. However, no obvious decrease of volumetric strain and porosity reduction after C' indicates that only small amount of dilatancy occurred for TCDP siltstone samples.

Figure 3.3 shows that at different effective pressures, the strength of siltstone increases with increasing effective pressure. As in the experiments with an effective pressure of 20 MPa, the mechanical response and failure modes of other siltstone samples deformed at effective pressures of 40 and 60 MPa are typical in the brittle faulting regime. Rock T837 has brittle strengths of 140 and 172 MPa at effective pressures of 40 and 60 MPa, respectively. The fracture strengths corresponding to brittle failure are obviously dependent on confining pressure. Therefore, samples are weaker while deformed at lower effective pressure. The stress-strain curve of samples deformed during linear elastic deformation shows that samples are more elastically compliant at lower effective pressure.

The Young's moduli of TCDP country rock samples are shown in Table 3.1. The values for the Young's modulus are on the order of 10 GPa, while the dry samples have higher values than wet ones. Several models with various distributions of elastic properties were used to infer the geometry of Chelungpu fault using finite source inversion with strong ground motion and GPS data (*Johnson and Segall*, 2004). Our laboratory data for TCDP samples provide useful constraints on the elastic moduli of the compliant surface layer, that was incorporated into recent inverse models that realistically agreed with GPS data for the Chi-Chi earthquake (*Ji et al.*, 2001 and 2003).

3.1.2 Failure Mode and Coefficient of Friction

The deformed samples show that the failure behaviors are different for siltstone (Figure 3.4a) and sandstone (Figure 3.4b). The shaly siltstone sample deformed to large strain develops multiple shear faults that are aligned almost exactly with the bedding

direction. So the small dilatancy observed in the shaly siltstone is probably related to the strong control of bedding on its failure mode. In contrast, the porous sandstone develops a mosaic of shear bands at different angles. The failure mode of siltstones is strongly controlled by bedding. Since the principal stresses for a triaxial compression test on samples cored in direction X simulate those in thrust faulting regime, and the failure mode of siltstones is characterized by planar shear faults aligned almost with the bedding direction, this implies that bedding anisotropy may have dominant control over the style of faulting.

Coefficients of friction are calculated from the residual frictional strength of siltstone samples after shear failure. The orientations of the parallel shear bands within the fractured samples are about 31° to 33°. Frictional coefficients are inferred to be 0.87, 0.71 and 0.68 corresponding to residual frictional strength of 90, 120 and 158 MPa for shaly siltstones T837 that were deformed at effective pressures of 20, 40 and 60 MPa, respectively (Table 3.1). However, siltstone T1248 has frictional coefficients of 0.92 to 0.94 corresponding to a residual frictional strength of 93 MPa deformed at an effective pressure of 20 MPa. Compared with TCDP fault core samples with which have frictional coefficients of 0.55 to 0.75 (*Lockner et al.*, 2005), the frictional coefficients in both country rocks and fault core are consistent with Byerlee's Law.

3.2 Permeability Data

Since our mechanical data show that presence of water could weaken the rock, the transport properties of fluid within a fault system can influence the rupture mechanics. Measurement of permeability would help us interpret the spatial variations of

hydromechanical behavior controlling the faulting process.

Two sandstones and three siltstones located at depths from 588 to 1248 m were tested. The permeabilities of sandstones with higher porosities were measured at different stages of deformation during the triaxial compression at an effective pressure of 20 MPa. For tight shaly siltstones, the permeabilities were only obtained during hydrostatic compaction.

The axial permeability data for hydrostatic loading and triaxial compression are compiled in Table 3.2 and 3.3, respectively. Shaly siltstone T837 with porosities of about 4 to 4.3 % have permeabilities as low as 10^{-16} to 10^{-19} m^2 during hydrostatic compression at effective pressures from 5 to 40 MPa. Figure 3.5a shows the permeability evolution with effective pressure for siltstone samples T837 that were cored in three directions. The figure indicates that the samples cored in direction Y are more permeable than those cored in direction X and Z. Since the permeability was too low to measure at higher effective pressure for siltstone T837, only permeabilities of one sample cored in direction Y (TC#15) were measured while triaxially deformed at an effective pressure of 20 MPa. Figure 3.5b shows that the permeability of TC#15 dropped dramatically by two orders of magnitude while reaching peak stress and increases slightly after the stress drop accompanying small amount of dilatancy.

The permeabilities of siltstone T1248 (TC#21) are comparable to those of T837 with values on the order of 10^{-16} to 10^{-19} m^2 (Figure 3.5c). T785 (TC#20) that has a higher porosity is the most permeable among three siltstones at various depths. The initial permeability for T785 was slightly higher than the other two siltstones at an effective pressure of 5 MPa, and it evolved to be higher by two orders of magnitude at an effective pressure of 40 MPa.

Permeabilities of sample T837 hydrostatically compacted measured by pulse transient technique are presented as a function of porosity (Figure 3.6a). The permeabilities are higher for samples cored in direction Y than those cored in the other two directions with the same porosities. Permeability is controlled by not only the porosity change but also the spatial distribution of bedding.

The permeability changes with effective pressure and porosity can be characterized by pressure sensitivity coefficient γ and porosity sensitivity exponent α, respectively. The decay of permeability as a function of effective pressure can be approximated by an exponential equation:

$$k = k_0 \exp\left[-\gamma\left(P_{eff} - P_0\right)\right] \tag{6}$$

where k is the permeability at the effective pressure P_{eff}, and k_o is the permeability at the reference effective pressure P_o selected to be 5 MPa in this study. The values of γ are about 0.07 to 0.23 for siltstone T837 (Table 3.4) and comparable to rocks from other boreholes and fault zones (Table 3.5). Higher values of γ commonly corresponding to rocks with more cracks would indicate the potential for maintenance of pore pressure excess due to continuous influx of fluid from the fault zone (*Rice,* 1992).

Figure 3.6a shows that the permeability decreases with reduced bulk porosity in a log-log plot. The permeability can be approximated as a power law with porosity:

$$k = k_0\left(\phi / \phi_0\right)^{\alpha} \tag{7}$$

where ϕ and ϕ_0 are the porosity corresponding to the permeabilities k and k_0, respectively. Higher values of porosity sensitivity exponent α indicate that the samples have larger permeability loss related to porosity reduction with elevated effective pressure. The exponent α of siltstone T837 was derived from the slopes of this log-log plot. Only the

points with approximately linear correlation in this permeability-porosity plot were used to determine the porosity sensitivity exponent α. There is no obvious correlation between the value of α and the initial porosity or coring direction. However, the exponent α is still much higher for TCDP siltstones in this study than that for protolith extracted from other boreholes and fault zones (Table 3.4 and 3.5).

Although having a wide range of values of coefficients for siltstone T837, there is a positive linear relation between the pressure and porosity sensitivity coefficients (Figure 3.6b). The value of the ratio between these two coefficients for siltstone T1248 is comparable with those for T837. On the other hand, the linear correlation of these two coefficients of siltstone T785 with higher porosity is similar to that of sandstones. According to the definition of these two sensitivity coefficients for permeability (eq. (6) and (7)), a linear relationship betweens two coefficients can be derived (*David et al.*, 1994):

$$\gamma = -\frac{\alpha}{\phi}\frac{d\phi}{dP} = \alpha\beta_{\phi} \tag{8}$$

where β_{ϕ} is the compressibility of pore space. Higher values of γ/α indicate that the pore space within this sample is relatively more compressible. *David et al.* (1994) concluded two line representing the lowest boundaries of tight and porous rocks corresponding to the value of γ/α equal to 4.4×10^{-4} /MPa and 3.3×10^{-3} /MPa, respectively. Figure 3.6b shows that siltstones T837 and T1248 with lower porosity 4 to 4.3 % are more compressible and fall into the region of tight rocks. On the other hand, siltstone T785 with a higher porosity of 6.65 % and sandstones are all located within the range of porous rocks bracketed by these two linear boundaries. Therefore, the permeabilities of TCDP siltstones with smaller porosity are more sensitive to pressure than those of more porous

rocks extracted from TCDP borehole.

3.3 Microstructural Observations

Not only the mechanical and permeability data of TCDP core samples but also the magnetic and seismic wave data obtained from the logging data in the field (*Hung et al.*, 2007) and measurements in laboratory reveal the characteristic of anisotropy (*Louis et al.*, 2008). The logging data collected from a Dipole Shear Sonic Imaging (DSI) in TCDP Hole-A indicate shear wave velocity anisotropy. The results at depths from 508 m to 1080 m can be grouped into nine separate intervals with similar directions of fast polarization.

In the laboratory, the anisotropy of magnetic susceptibility (AMS) and anisotropy of P-wave velocity (APV) in nine siltstone and six sandstone samples retrieved from TCDP Hole-A at depths ranging from 589 to 1412 m were characterized (*Louis et al.*, 2008). The data show that the AMS were similar for all samples regardless of lithologic facies, with the principal direction of the minimum magnetic susceptibility K_{min} located near the pole of the bedding plane, while the directions of the maximum and intermediate magnetic susceptibility K_{max} and K_{int} fell into two clusters aligned near the bedding plane (Figure 3.7a). The magnetic fabric of these samples indicates that these weakly deformed sedimentary rocks have undergone layer parallel shortening.

On the other hand, the acoustic experiments reveal that the elastic fabric is sensitive to the lithology. The distribution of principal directions of the maximum, intermediate and minimum P-wave velocity, V_{max}, V_{int} and V_{min}, were different for TCDP siltstone (Figure 3.7b) and sandstone (Figure 3.7c) samples. In siltstones, the direction of V_{min} is in the vicinity of the pole of the bedding plane, similar to the AMS data. This suggests that

the APV is strongly influenced by preferred alignment of clay minerals. However the APV data for sandstones show that the orientation of V_{min} is subparallel to the strike of the bedding, while the V_{max} is subparallel to the bedding dipping direction and V_{int} is near the bedding pole (Figure 3.7c). The measurements of the P-wave velocity differences between nominally dry and water-saturated samples were used to investigate the relation of pore space anisotropy to the APV results in sandstones. The velocity contrast data (Figure 3.7d) indicate that the maximum velocity differences are in the direction parallel to the strike of the bedding, while the minimum velocity differences were close to the bedding direction.

Microstructural observations were performed to characterize the distribution of pore space and microcracks. The micrographs of intact siltstone T837 and sandstone T588 taken under an optical microscope with transmitted light at a magnification of 50× are shown in Figure 3.8a and b, respectively. In the siltstone sample, the contrast in grain size between the very fine clay minerals inside the bedding and the relatively coarser quartz grains outside (Figure 3.8a) were identified. In contrast, the grain size was larger and more pervasive intragranular microcracking was observed in the grain-supported sandstone (Figure 3.8b). Characterizing the orientations and lengths of microcracks provided constraints on the magnitude and anisotropy of P-wave velocity.

The microcracks are distributed with preferential orientation in each thin section (Figure 3.9a to c), this is particularly obvious in the X and Z sections for the three sandstones. Meanwhile, the microcracking is more intense in the X and Z sections than that in the Y sections for all three TCDP sandstone samples. Totally, more than ninety thousands microcracks were traced in nine thin sections from 3 TCDP sandstones and were mapped on the images followed by measurements of the statistical distributions of

the orientations and lengths of microcracks. To minimize the statistical error, the intragranular microcracks with length less than 20 pixel were eliminated while dealing with orientation data.

To determine the anisotropy of microcrack distribution, the orientations of cracks were grouped into bins of 10°. The quantities and lengths of microcracks with orientations that fell within each 10° interval are plotted in polar diagrams (Figure 3.10, 3.11 and 3.12). The orientation data obtained from software ImageJ was bi-directional data that could represent crack orientation measured in either of two directions differed by 180° (for example, 90° to 100° and 270° to 280°), so the total numbers of microcracks in each interval were distributed equally into the corresponding orientation intervals and the intervals differed by 180°. The polar plots show that the microcracks in Z section are preferentially aligned with azimuth N105°E for the three sandstones. However, the cracks in sandstone T1365 (Figure 3.11) and T1394 (Figure 3.12) have similar preferred orientations in X, Y sections, but the preferential orientation in X section of sandstone T850 is subparallel to the TCDP core axis which is different from those in the other two sandstone samples.

Stereological measurements of the linear intercept density were performed in order to characterize the anisotropic distribution of microcracks. The maximum intercept density orientation is perpendicular to the preferential orientation of microcracks. Figure 3.13 displays the correlation between the orientation data and intercept density of microcracks. Since the increment of angle for intercept density measurements is more precise than the bin of grouping orientation data, the preferential orientation on each thin section is obtained from the minimum intercept density orientation (Table 3.6).

The orientations of microcracks in three mutually perpendicular sections can be

considered as the projections of planar discontinuities on three orthogonal planes. The preferential orientations of microcracks in three orthogonal sections can constrain the planes that represent a best-fit approximation to the preferentially oriented cracks in three-dimension. It is very important to correlate the orientation data of microcracks obtained from the thin sections with the geographic orientation. For X sections, the orientation data in the polar plots is meant to be viewed from N105°E, and the orientation N15°E and N195°E in polar plots is donated by 180° and 0° on the images. For Y sections, the orientation data in the polar plots is meant to be viewed from N15°E, and the orientation N105°E and N285°E in polar plots is donated by 0° and 180° on the images. For Z sections, the orientation data in the polar plot is viewed from the top of the TCDP core axis, and 0°, 90°, 180°, and 270° represent the N15°E, N105°E, N195°E and N285°E directions, respectively.

The preferentially oriented crack planes and normals to the crack planes of three sandstone samples are then determined and plotted on an equal-area lower hemispheric stereonet, using the code developed by *R. Allmendinger* (Figure 3.14). The preferential crack planes in three TCDP sandstones are subperpendicular to the strike of the bedding with higher dipping angles. The poles of the preferential crack plane located parallel to the azimuth of the strike of the bedding at a very small angle with respect to the horizon are also shown in Figure 3.14.

The results of P-wave velocity anisotropy of three TCDP sandstones are displayed on the stereonet with preferential crack planes and poles of the crack planes in the three sandstones for comparison (Figure 3.14). Comparing the microcrack fabric with seismic anisotropy data, it is obvious that the directions of the fast P-wave are subparallel to the preferred orientations of the microcrack planes and the poles of the microcrack planes are

highly consistent with the orientations of the minimum P-wave velocities. This implies that there is a set of parallel crack planes aligned almost along the azimuth N105°E with a right angle to the horizon that reduce seismic wave while propagating perpendicular to the crack planes in TCDP sandstones.

The in-situ stresses at the drilling site were also inferred from borehole breakouts and drilling-induced tensile fractures (*Hung et al.*, 2007; *Wu et al.*, 2007). The direction of regional maximum horizontal principal stress (S_{Hmax}) acquired from the breakout data is N115°E, which is slightly different from the preferential orientations of microcrack planes in the sandstones (N105°E). However, the average bedding dipping direction in TCDP Hole-A (*Yeh et al.*, 2007) and paleostress trajectory derived from fold axes and fault analysis (*Angelier et al.*, 1986) were much closer to the orientations of the preferred crack planes. This suggests that microcrack anisotropy in TCDP sandstones might be related to the paleostress field.

3.4 Factors Control Anisotropy in Two Facies

Anisotropies of mechanical, permeability, magnetic and seismic properties were observed in country rocks retrieved from TCDP Hole-A. For siltstones, the anisotropies of mechanical strength and permeability in this study are significantly controlled by the distribution of bedding. Samples cored along the orientation N105°E (sample X) have higher brittle strengths than those cored parallel to the TCDP core axis (sample Z) by about 10 MPa. The small amount of dilatancy observed in the shaly siltstones is probably related to the strong control of bedding on their failure mode. Multiple parallel shear bands aligned almost exactly with the bedding direction were developed within siltstones

that were deformed to large strain.

The results of permeability measurement show that the samples cored along direction Y which is parallel to the strike of bedding are more permeable than those cored in the other two directions. The bedding plane is 30° with respect to the direction of the maximum principal stress in samples cored in X direction and 60° in those cored in Z direction (Figure 2.2b), and the bedding planes within samples that were cored in direction Y are parallel to the direction of the maximum principal stress that facilitate the transportation of fluid flowing along the axial direction.

The magnetic susceptibility and P-wave velocity data were also consistent while the minimal susceptibility and wave velocity were clustering near the vicinity of the pole of the bedding plane for siltstones. These observations lead to the conclusion that the magnetic and elastic fabrics were controlled by the preferential alignment of clay minerals along the bedding plane within TCDP siltstones.

For TCDP sandstones, the results of mechanical strength show similar characteristic of anisotropy. Sandstone sample T588 cored along direction X is slightly stronger than that cored in direction Z. The brittle strength difference between samples cored in these two directions may not only be dominated by the bedding orientation with respect to the maximum principal stress but the distribution of pore space as well. The microstructural observation has revealed that the crack anisotropy exists in the TCDP sandstones. There are preferentially orientated microcracks planes subvertical with azimuth N105°E with poles subparallel to the orientation of minimum P-wave velocity while the direction of the maximum P-wave velocity are along the crack planes. This anisotropy of microcrock orientation could cause the elastic and magnetic anisotropy in TCDP sandstones.

3.5 Implication for Thermal Pressurization as a Mechanism of Fault Weakening

According to our laboratory measurement of TCDP shaly siltstone samples, if we take the permeability as 10^{-18} to 10^{-17} m^2 and porosity as 0.037, then the hydraulic diffusivity would be about 10^{-4} to 10^{-3} m^2/s, which is lower than the critical diffusivity value suggested by *Andrews* (2002) by orders of magnitude. It should also be pointed out that the data of *Locker et al.* (2005) for TCDP fault gouge with permeability about 10^{-20} m^2 indicated even lower diffusivity value, comparable to what *Andrews* (2002) suggested. Since the frictional strengths of the TCDP country rocks and gouge samples are comparable to Byerlee's Law, thermal pressurization of pore fluid would be expected in the TCDP shaly rocks and may provide a mechanism for dynamic weakening of Chelungpu fault. The threshold propagation distance that is derived from our calculation of the hydraulic diffusivity for shaly samples is significantly less than 300 m which was estimated by *Andrews* (2002). This result suggests that the location where the thermal pressurization effect would become more important was much closer to the main slip zone in the Chi-Chi earthquake event.

Table 3.1 Compilation of mechanical data.

Sample Number	Depth & Orientation	Saturation State	Effective Pressure (MPa) $P_c - P_p$	Peak Differential Stress (MPa) $\sigma_1 - \sigma_3$	Peak Effective Mean Stress (MPa) $(\sigma_1 + 2\sigma_3)/3 - P_p$	Axial Strain ε (%)	Coefficient of Friction	Young's modulus E (GPa)
Siltstone								
TC#02	T837-Z	Dry	20	160.3	73.6	4.74		16.3
TC#03	T837-X	Dry	20	170.8	77.1	4.46		19.9
TC#04	T837-Z	Dry	20	162.7	74.1	1.29		
TC#05	T837-X	Wet	20	115.5	58.8	3.87	0.87	5.9
TC#06	T837-Z	Wet	20	109.9	57.2	4.37	0.88	4.5
TC#13	T837-X	Wet	40	122.1	80.9	5.40	0.68	4.7
TC#14	T837-Z	Wet	40	140.3	87.2	4.78	0.74	5.1
TC#16	T837-Z	Wet	60	172.1	118.2	7.52	0.68	6.4
TC#22	T1248-X	Wet	20	117.6	59.5	3.47	0.93	5.7
Sandstone								
TC#09	T588-Z	Wet	20	106.6	57.2	3.72		7.0
TC#10	T588-X	Wet	20	116.4	59.2	3.56		7.9

Table 3.2 Compilation of permeability data for hydrostatic tests.

Sample Number	Depth & Orientation	Effective Pressure (MPa) P_c - P_p	Porosity ϕ (%)	Permeability k (m^2)
Siltstone				
TC#07	T837-X	5.3	4.0	1.3×10^{-18}
		11.5	4.0	1.8×10^{-18}
		21.3	3.8	1.4×10^{-18}
		31.0	3.6	5.9×10^{-19}
		41.1	3.5	2.3×10^{-19}
TC#08	T837-Y	6.6	4.0	1.7×10^{-17}
		10.0	3.9	2.0×10^{-17}
		20.4	3.7	7.6×10^{-18}
		30.3	3.4	3.1×10^{-18}
		40.8	3.2	9.6×10^{-19}
		31.8	3.2	1.6×10^{-18}
		22.0	3.2	3.4×10^{-18}
TC#11	T837-Z	6.3	4.3	4.7×10^{-17}
		10.8	4.2	2.9×10^{-17}
		20.6	4.1	2.8×10^{-18}
TC#17	T837-X	5.8	4.3	1.3×10^{-16}
		11.3	4.3	6.1×10^{-17}
		20.9	4.2	3.5×10^{-18}
		31.5	4.0	3.3×10^{-19}
		41.3	3.9	5.4×10^{-20}
TC#18	T837-X	6.8	4.2	4.2×10^{-17}
		10.8	4.2	1.9×10^{-18}
		22.1	3.9	9.1×10^{-19}
		31.1	3.8	3.1×10^{-19}
		41.9	3.5	1.2×10^{-19}

Table 3.2 Continued

Sample Number	Depth & Orientation	Effective Pressure (MPa) P_c - P_p	Porosity ϕ (%)	Permeability k (m^2)
Siltstone				
TC#20	T1248-X	5.5	4.0	6.5×10^{-17}
		10.4	4.0	3.0×10^{-17}
		20.5	3.8	4.0×10^{-18}
		30.7	3.6	5.3×10^{-19}
TC#21	T785-X	6.4	6.6	2.0×10^{-16}
		10.9	6.6	1.7×10^{-16}
		21.3	6.4	1.2×10^{-16}
		31.3	6.3	7.9×10^{-17}
		41.0	6.2	5.3×10^{-17}
		50.6	6.2	3.1×10^{-17}
		60.4	6.2	1.1×10^{-17}
		70.9	6.1	5.3×10^{-18}
		80.9	6.0	1.8×10^{-18}
		91.3	5.9	9.8×10^{-19}
		101.7	5.7	3.8×10^{-19}

Table 3.3 Compilation of permeability data for triaxial tests.

Sample Number	Depth & Orientation	Effective Pressure (MPa) P_c - P_p	Differential Stress (MPa) σ_1 - σ_3	Porosity ϕ (%)	Axial Strain ε (%)	Permeability k (m^2)
Siltstone						
TC#15	T837-Y	6.4	0.0	3.99		1.2×10^{-15}
		21.0	0.0	3.74	0.00	6.4×10^{-17}
		20.9	59.9	3.55	1.13	1.7×10^{-18}
		21.0	92.6	3.55	2.88	1.3×10^{-19}
		21.0	94.9	3.57	4.27	1.4×10^{-19}
Sandstone						
TC#12	T588-Y	6.3	0.0	15.88		3.1×10^{-14}
		11.3	0.0	15.76		9.7×10^{-15}
		15.4	0.0	15.75		6.8×10^{-15}
		20.4	0.0	15.42	0.00	3.3×10^{-15}
		20.5	43.8	14.82	1.14	8.3×10^{-16}
		20.8	74.3	14.66	1.87	5.0×10^{-16}
		20.3	92.3	14.64	2.31	2.2×10^{-16}
		21.5	108.6	15.00	3.65	5.7×10^{-18}
		20.7	102.7	15.33	4.83	6.4×10^{-18}
		21.0	110.3	15.43	5.89	8.1×10^{-18}
TC#19	T850-X	5.2	0.0	18.56		5.2×10^{-14}
		10.5	0.0	18.41		5.0×10^{-14}
		15.2	0.0	18.22		3.0×10^{-14}
		20.3	0.0	17.99	0.00	2.9×10^{-14}
		20.6	60.9	17.51	0.91	9.8×10^{-15}
		20.6	109.1	17.41	1.71	3.8×10^{-15}
		20.5	126.4	17.69	2.45	2.1×10^{-15}
		20.2	84.8	18.01	3.66	1.9×10^{-15}
		20.9	92.9	18.03	5.76	1.3×10^{-15}

Table 3.4 Effective pressure sensitivity and porosity sensitivity exponent for TCDP siltstones.

Sample Number	$k = k_0 \exp[-\gamma(P_{eff} - P_0)]$		$k = k_0 (\phi / \phi_0)^{\alpha}$		Pore Compressibility
	γ (MPa^{-1})	k_0 (m^2)	α	ϕ_o (%)	10^{-3} MPa^{-1}
Siltstone					
TC#07	0.078	2.0×10^{-18}	18.4	3.9	4.2
TC#08	0.098	2.0×10^{-17}	14.1	3.9	6.9
TC#11	0.202	4.7×10^{-17}	60.9	4.3	3.3
TC#15	0.199	1.2×10^{-15}	45.4	4.0	4.4
TC#17	0.228	1.3×10^{-16}	66.3	4.3	3.4
TC#18	0.091	1.9×10^{-18}	16.2	4.2	5.6
TC#20	0.193	6.5×10^{-17}	42.1	4.0	4.6
TC#21	0.041	2.0×10^{-16}	24.5	6.6	1.7
	0.085	3.1×10^{-17}	50.8	6.2	1.7
Sandstone					
TC#12	0.155	3.1×10^{-14}	66.1	15.9	2.3
TC#19	0.045	5.2×10^{-14}	21.7	18.6	2.1

Table 3.5 Compilation of pressure and porosity sensitivity of permeability for different rocks in fault zones.

Material Type	γ [MPa^{-1}]	α	Reference
gneiss (Kola)	0.032		*Morrow et al.*, 1994
basalt (Kola)	0.106		*Morrow et al.*, 1994
amphibolite (KTB)	0.058 - 0.116		*Morrow et al.*, 1994
granodiorite (Cajon Pass)	0.127		*Morrow and Lockner*, 1994
East Fort thrust fault, Wyoming			*Evans et al.*, 1997
protolith	0.165 - 0.2		
Dixie Valley normal fault			*Seront et al.*, 1998
protolith	0.04 - 0.152	53.48	

Table 3.6 Orientation data for microcracks.

Sample Number	Section	Total crack counted	Average length (micron)	Preferential orientation	Best-fit crack plane	Pole of crack plane
T850	X	13857	94.9	N15°E, 89°N	N101.1°E, 89.5°S	N11.1°E, 0.5°N
	Y	2978	106.7	N105°E, 55°E		
	Z	5535	121.1	N100°E, 0°		
T1365	X	15381	67.5	N15°E, 81°N	N285.5°E, 84.3°N	N195.5°E, 5.7°S
	Y	4700	93.5	N105°E, 53°E		
	Z	8777	90	N103°E, 0°		
T1394	X	16564	74.4	N15°E, 71°N	N288.3°E, 77.1°N	N198.3°E, 12.9°S
	Y	10087	95.7	N105°E, 51°E		
	Z	13362	94.1	N103°E, 0°		

a)

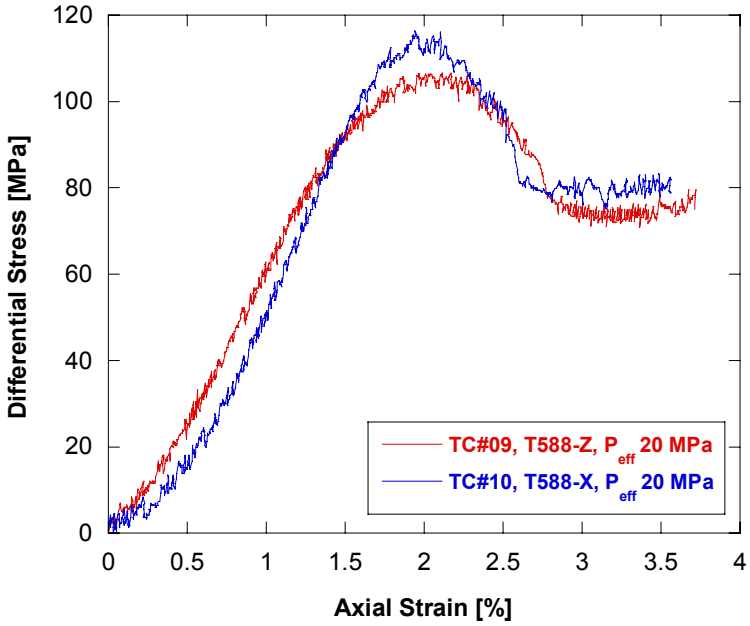

b)

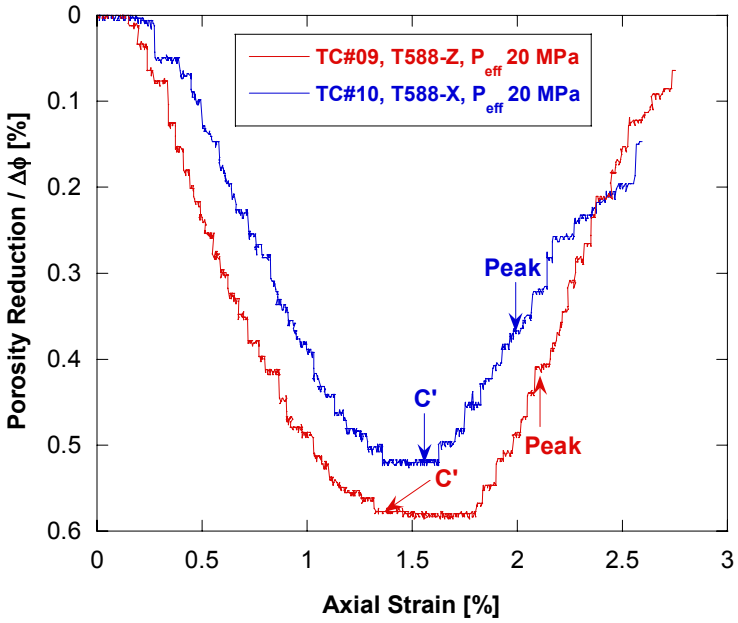

Figure 3.1 Mechanical data of sandstone T588 cored in direction X (blue) and Z (red). a) Differential stress as a function of axial strain. T588-X is slightly stronger than T588-Z deformed at an effective pressure of 20 MPa. b) Porosity reduction as a function of axial strain. Dilatancy was observed after C' in both samples.

a)

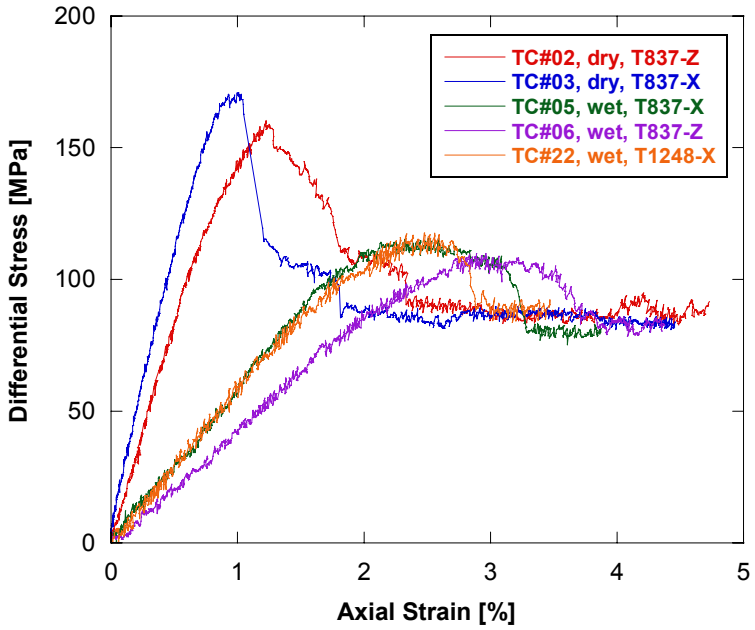

b)

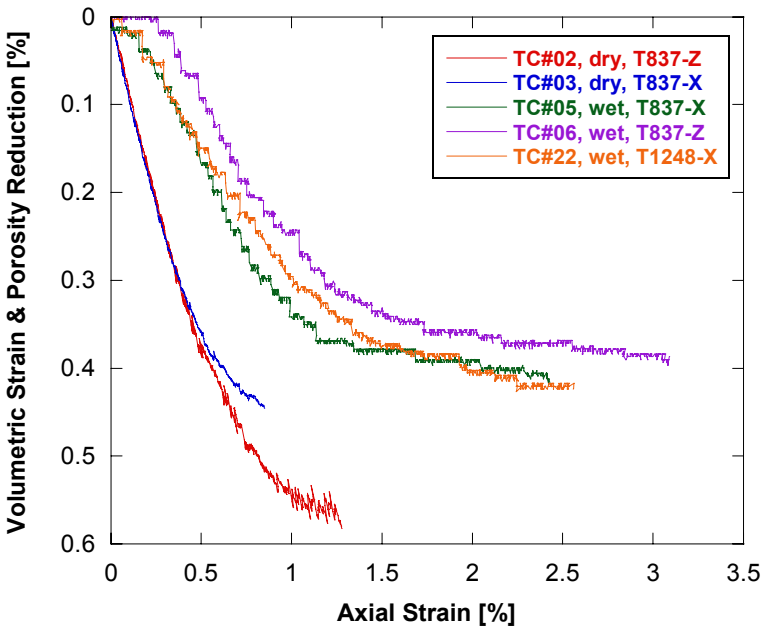

Figure 3.2 Mechanical data of siltstone T837 and T1248. a) Differential stress as a function of axial strain. T837-X is slightly stronger than T837-Z deformed at an effective pressure of 20 MPa under both dry and wet conditions. b) Volumetric strain and porosity reduction as functions of axial strain. No obvious dilatancy was observed in all samples.

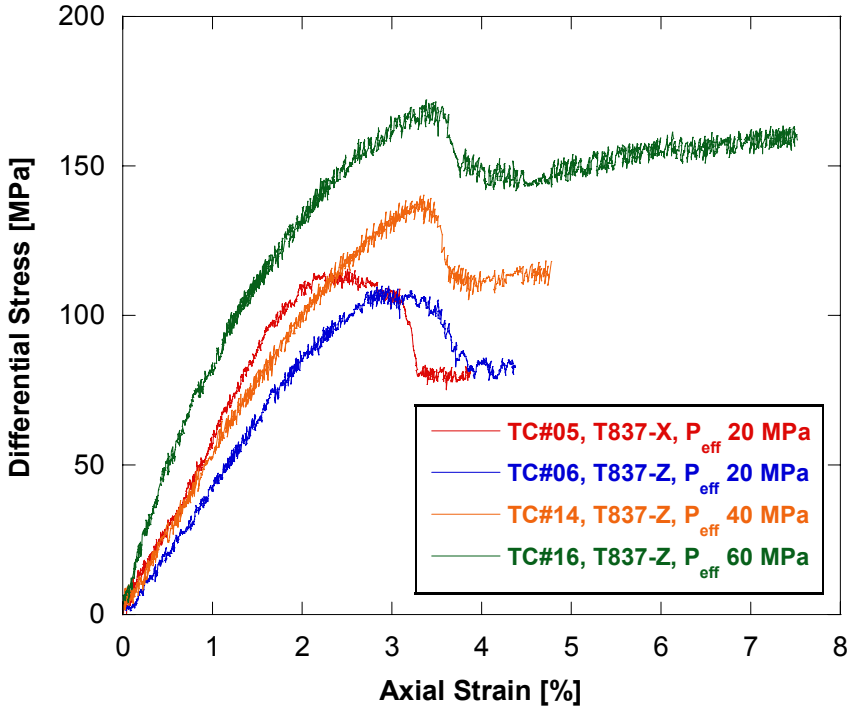

Figure 3.3 Differential stress as a function of axial strain for T837 deformed at various effective pressures. The mechanical response is brittle failure for all samples deformed at effective pressures of 20, 40 and 60 MPa. The brittle strengths of the samples are higher while deformed at higher effective pressures.

a)

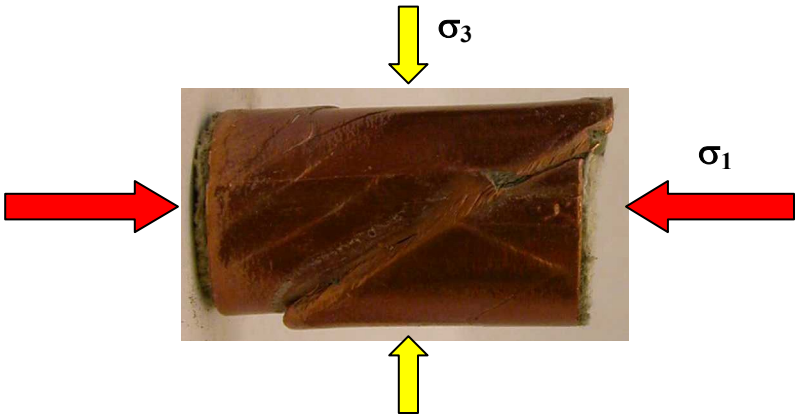

b)

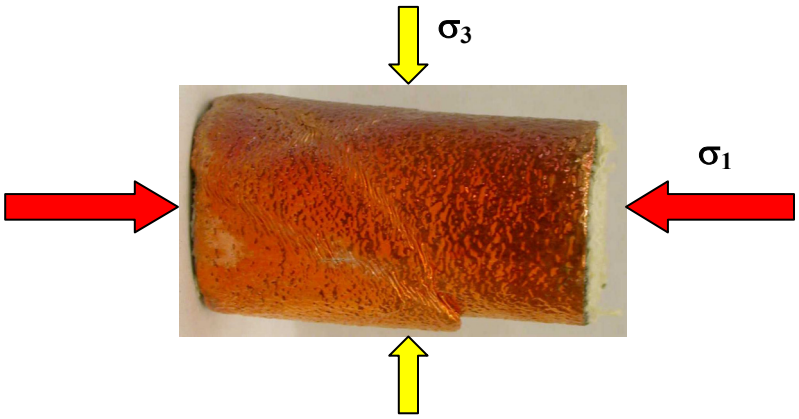

Figure 3.4 Photographs of fractured samples. a) The shaly siltstone sample deformed to large strain develops multiple shear faults that are aligned almost exactly with the bedding direction. b) The porous sandstone developed a mosaic of shear bands at different angles.

a)

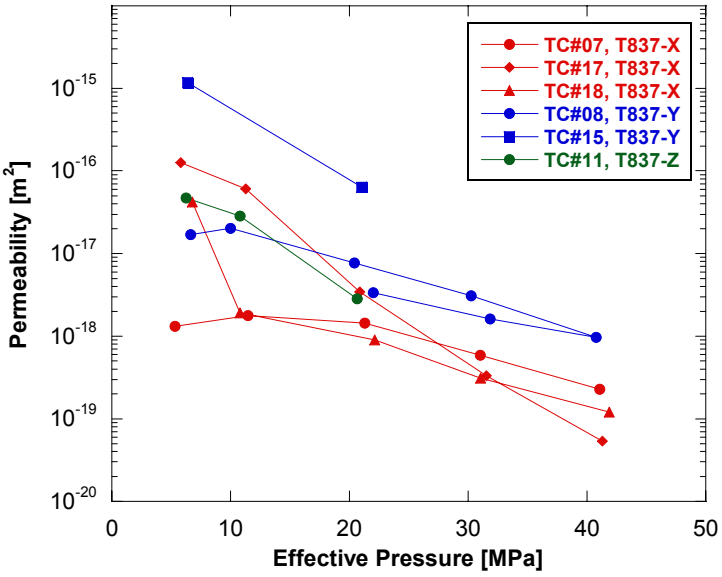

b)

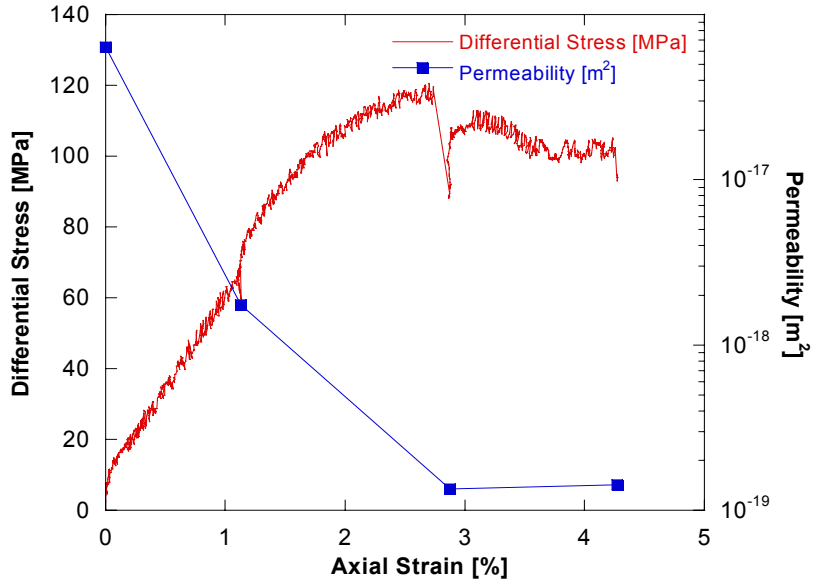

Figure 3.5 a) Permeability evolution with effective pressure of siltstone T837 compacted hydrostatically. Data of samples cored in direction X, Y and Z are shown in red, blue and green, respectively. Overall, Y samples are more permeable than X and Z samples. b) Permeability evolution and differential stress with axial strain of T837-Y (TC#15) compressed triaxially. The permeability dropped dramatically by two orders of magnitude while reaching peak stress and increased slightly after the stress drop accompanying small amount of dilatancy.

c)

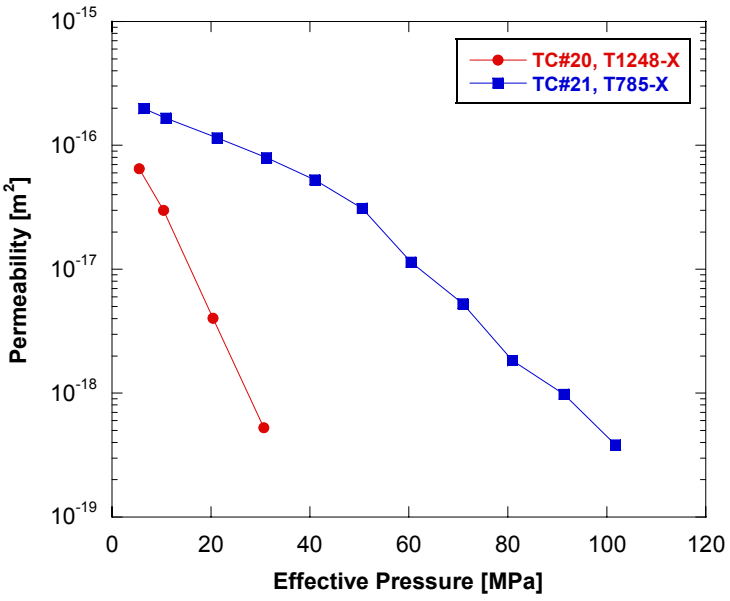

Figure 3.5 c) Permeability evolution with effective pressure of siltstone T785 and T1248 compacted hydrostatically. Data of samples T785-X and T1248-X are shown in blue and red, respectively. The permeability drop with effective pressure is faster in T1248-X than in T785-X. The permeability evolution with effective pressure in T1248-X is similar to that in T837-X (Figure 3.5a).

a)

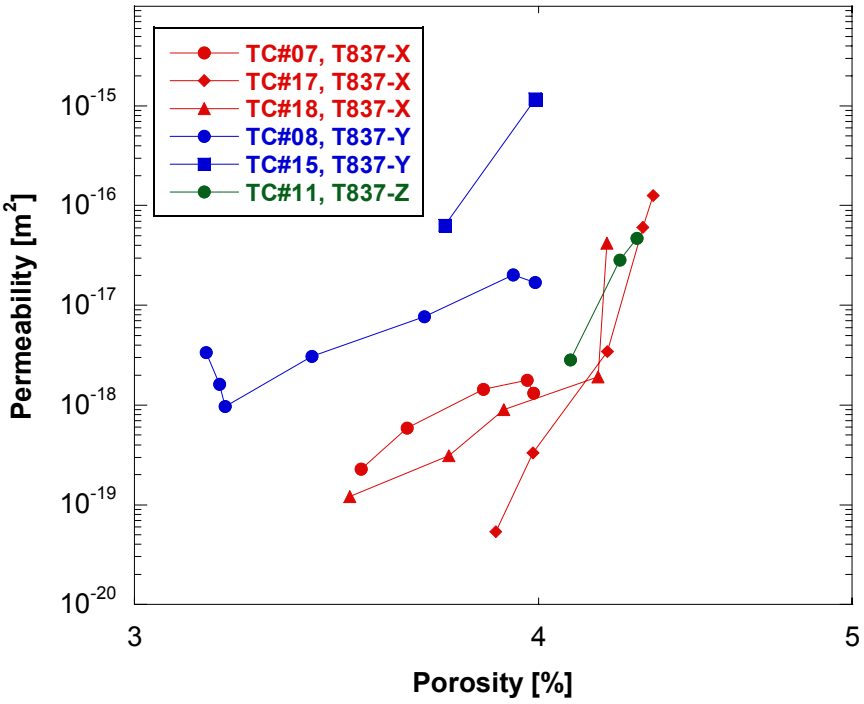

Figure 3.6a Permeability as a function of porosity in siltstone T837. All samples are compacted hydrostatically. The permeability decreases with reduced bulk porosity in a log-log plot. The porosity sensitivity exponent α can be derived from this plot according to the power law. Higher values of α indicate that the samples have larger permeability loss related to porosity reduction with elevated effective pressure.

b)

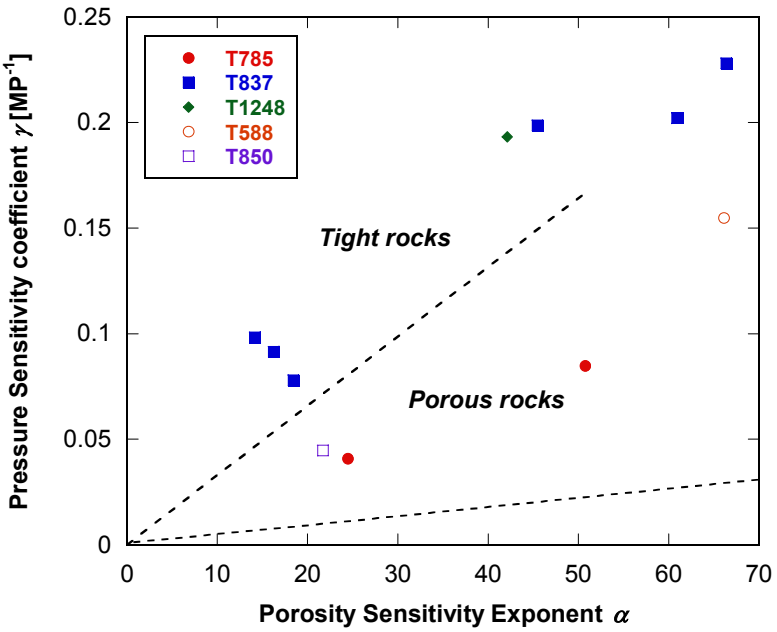

Figure 3.6b Correlation between the pressure sensitivity coefficient γ and the porosity sensitivity exponent α for shaly samples. Siltstones T837 and T1248 are more compressible and fall into the region of tight rocks. Siltstone T785 with a higher porosity and all sandstones are located within the range of porous rocks bracketed by these two linear boundaries. Two dashed lines represent the lowest boundaries of tight and porous rocks corresponding to the value of γ/α equal to 4.4×10^{-4} /MPa and 3.3×10^{-3} /MPa, respectively (*David et al.*, 1994).

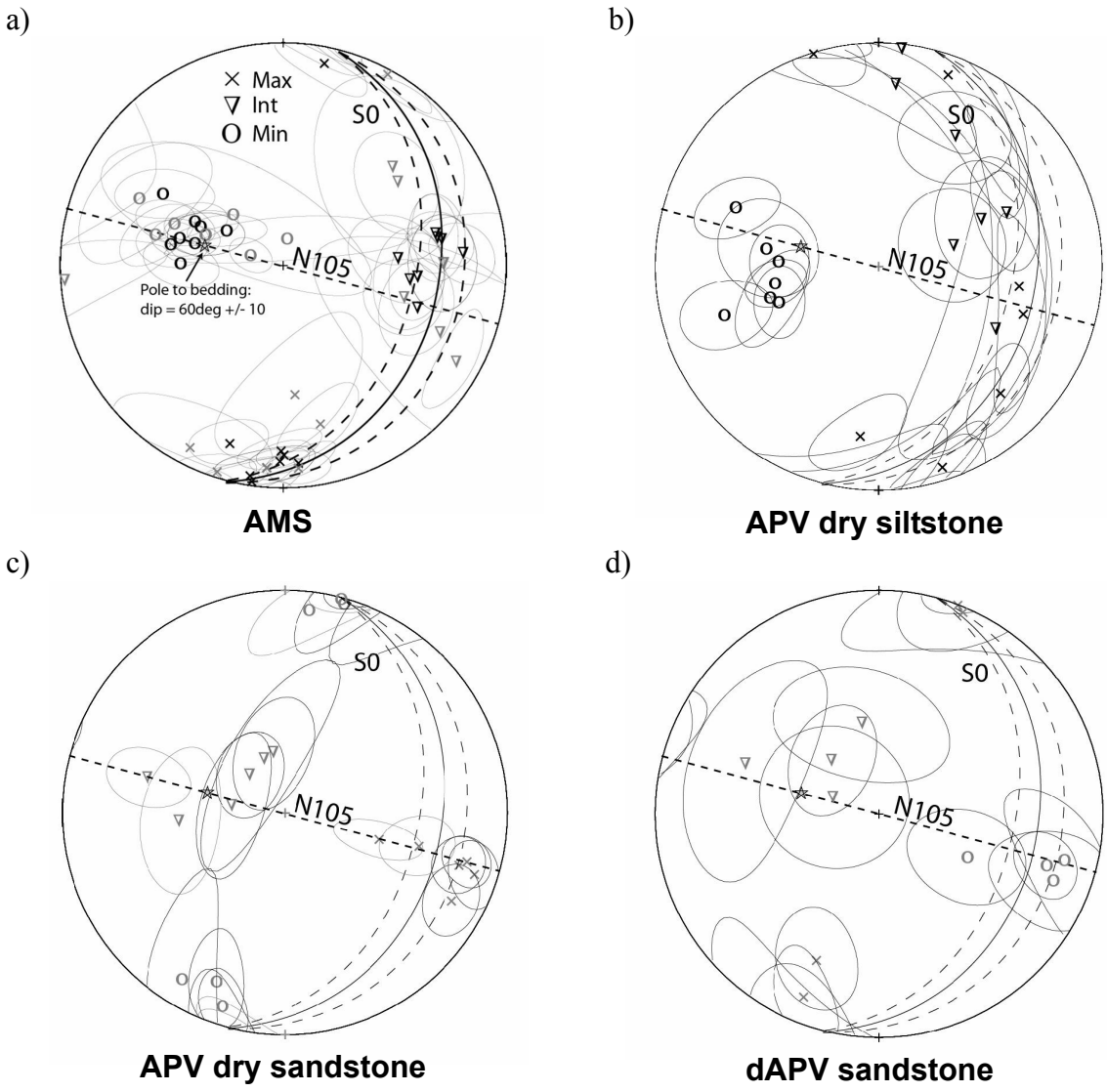

Figure 3.7 Equal-area lower hemispheric projection of anisotropy of magnetic susceptibility (AMS) and P-wave velocity (APV) (*Louis et al.*, 2008). a) AMS of TCDP samples. Black circles are sandstone and gray ones are siltstones. The data fall within three distinct clusters with the maximum parallel to the strike of the bedding and the minimum parallel to the normal of the bedding plane. b) APV of dry siltstones. The minimum is parallel to the normal of the bedding plane similar to the magnetic fabric and the intermediate and maximum scatter along the bedding plane. c) APV of dry sandstones. The data fall within three distinct clusters with the maximum parallel to the strike of the bedding and the minimum parallel to the normal of the bedding plane. d) Velocity difference data derived from P-wave velocity contrast (dAPV) between saturated and dry sandstones. The directions of maximum velocity differences are subparallel to the strike of the bedding.

a)

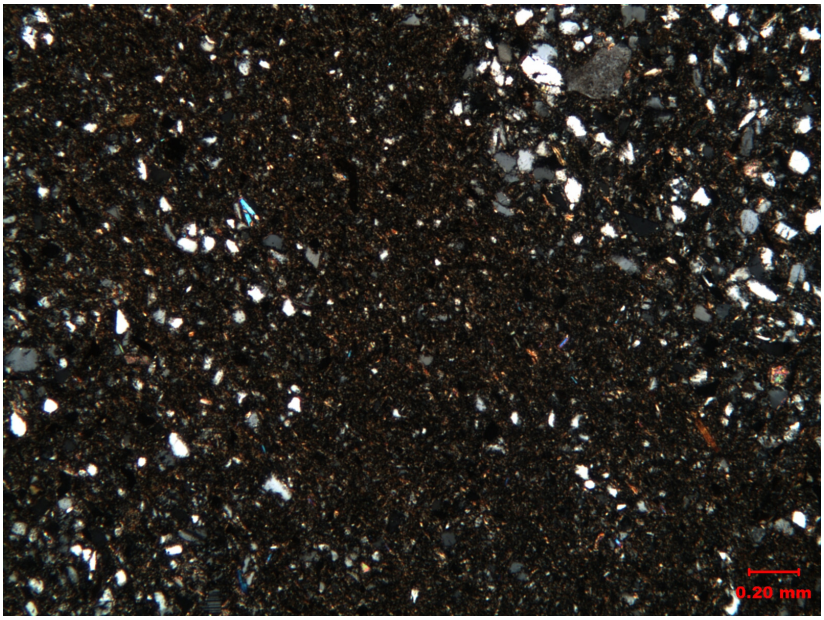

b)

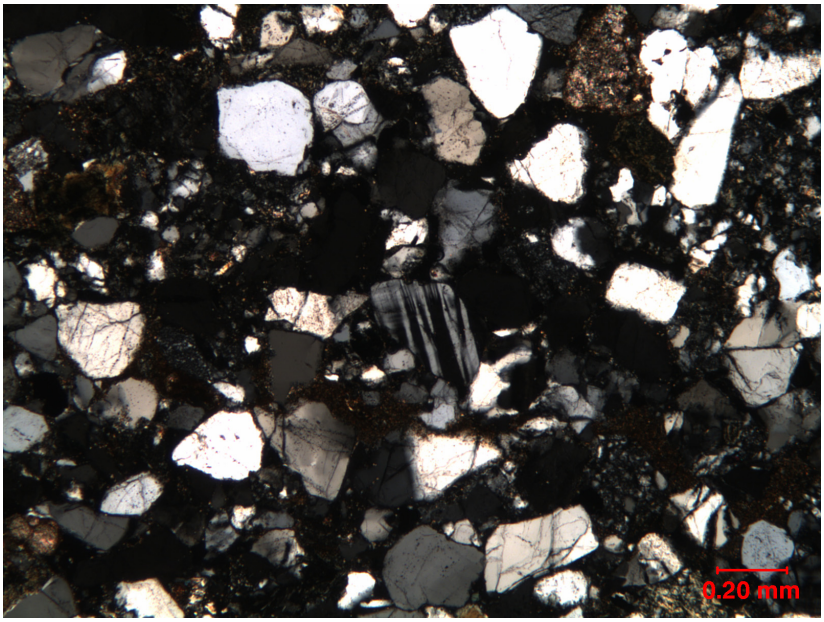

Figure 3.8 Micrograph of samples for comparison of microstructures between siltstone and sandstone. The scale bar is 0.2 mm. a) In siltstone, there is obvious contrast in grain size between the very fine clay minerals inside the bedding and coarser grains outside. b) The structure in the sandstone is grain-supported with intragranular microcracking.

a)

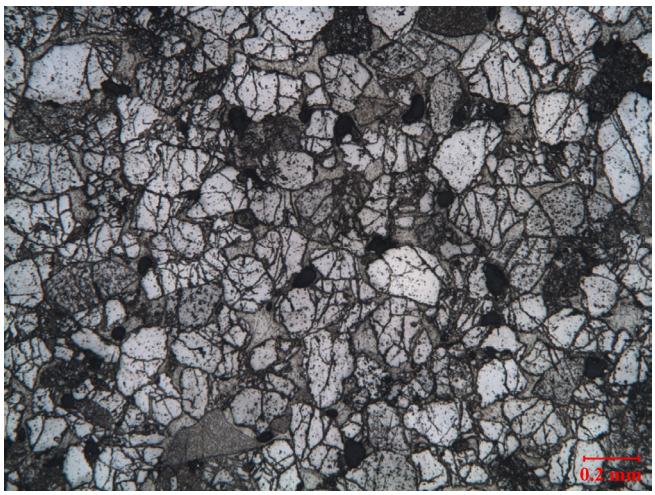

b)

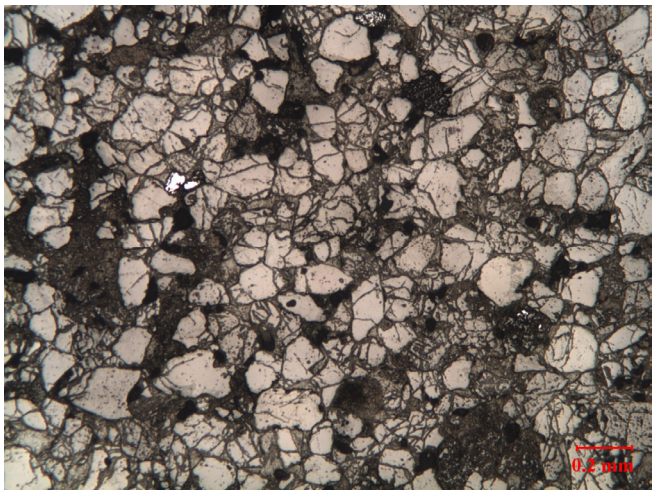

c)

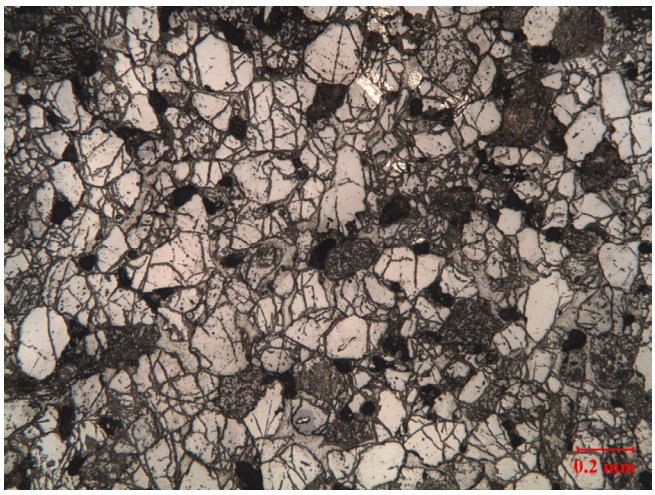

Figure 3.9 Microcracks distribution of sandstone T850 in three orthogonal sections. X, Y and Z sections are cut cross the coring direction X, Y and Z, respectively. a) T850-X section. b) T850-Y section. c) T850-Z section. Microcracsking is more intense in X and Z section than that in Y sections.

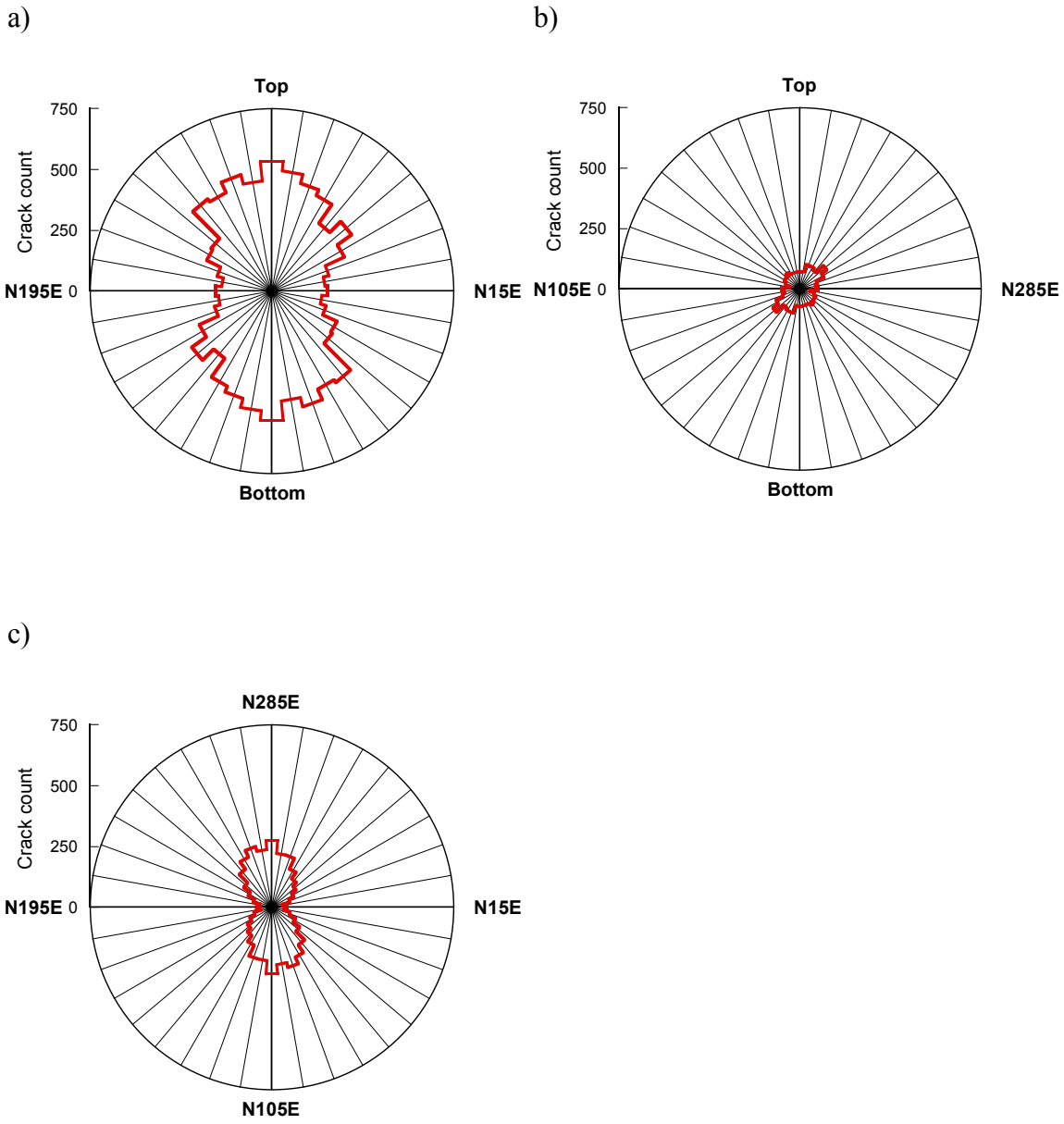

Figure 3.10 Polar plots of crack orientation in sandstone T850 obtained from three thin sections. a) The preferential orientation of microcracks in section T850-X is vertical. b) The preferential orientation of microcracks in section T850-Y is N105˚E, 40˚E. c) The preferential orientation of microcracks in section T850-Z is N105˚E, 0˚.

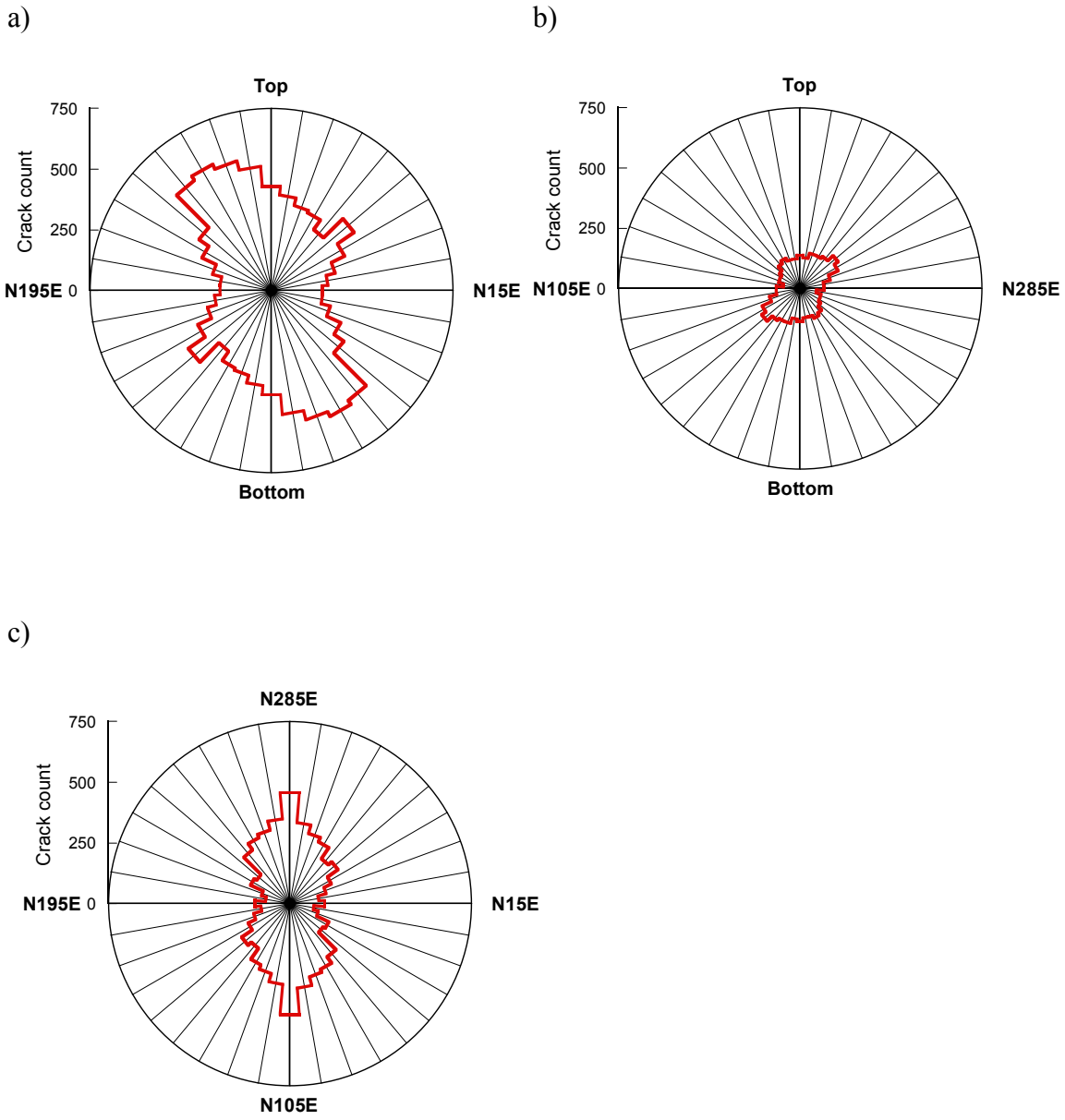

Figure 3.11 Polar plots of crack orientation in sandstone T1365 obtained from three thin sections. a) The preferential orientation of microcracks in section T1365-X is N15˚E, 60˚N. b) The preferential orientation of microcracks in section T1365-Y is N105˚E, 40˚E. c) The preferential orientation of microcracks in section T1365-Z is N105˚E, 0˚.

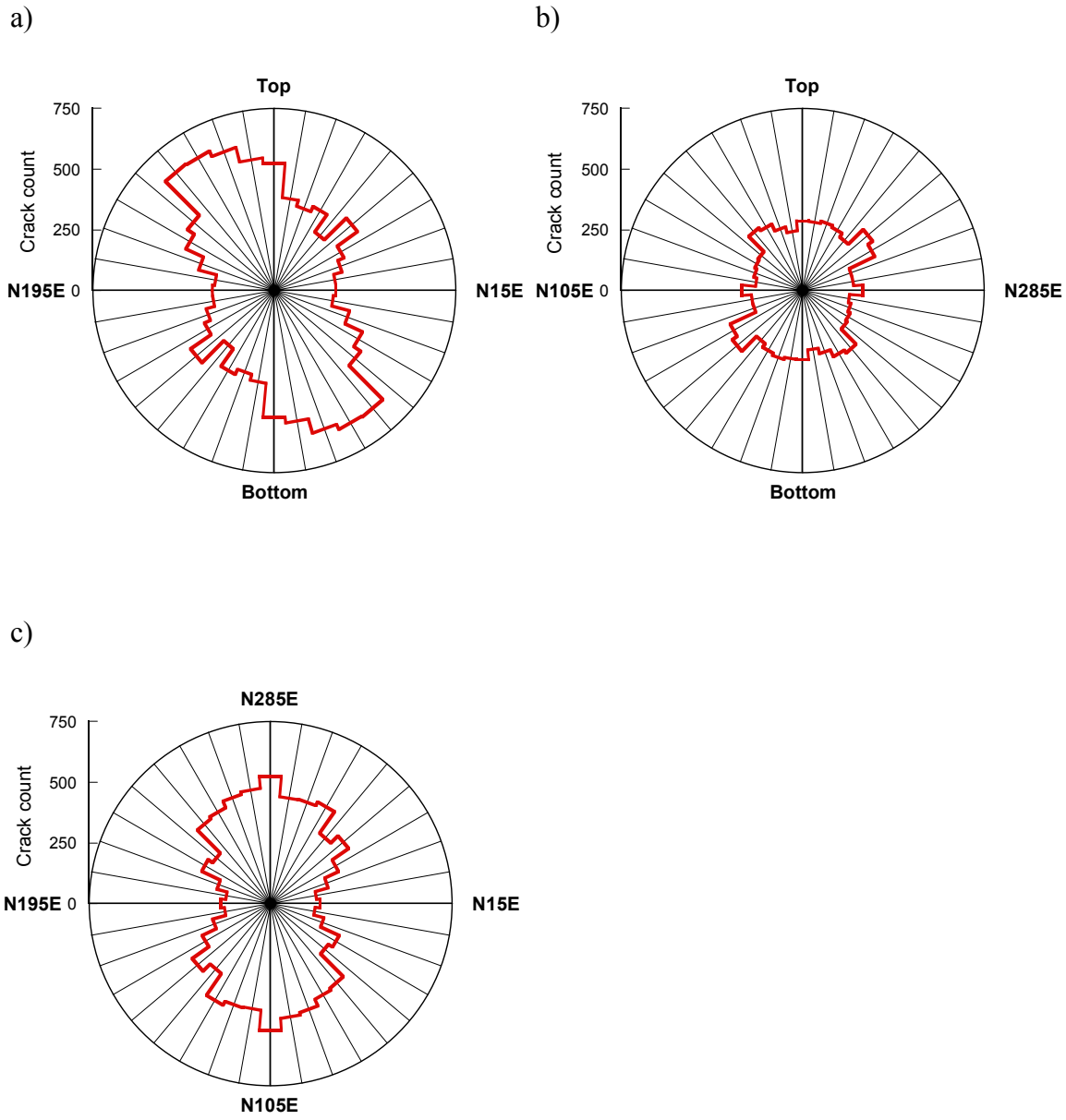

Figure 3.12 Polar plots of crack orientation in sandstone T1394 obtained from three thin sections. a) The preferential orientation of microcracks in section T1394-X is N15˚E, 55˚N. b) The preferential orientation of microcracks in section T1394-Y is N105˚E, 40˚E. c) The preferential orientation of microcracks in section T1394-Z is N105˚E, 0˚.

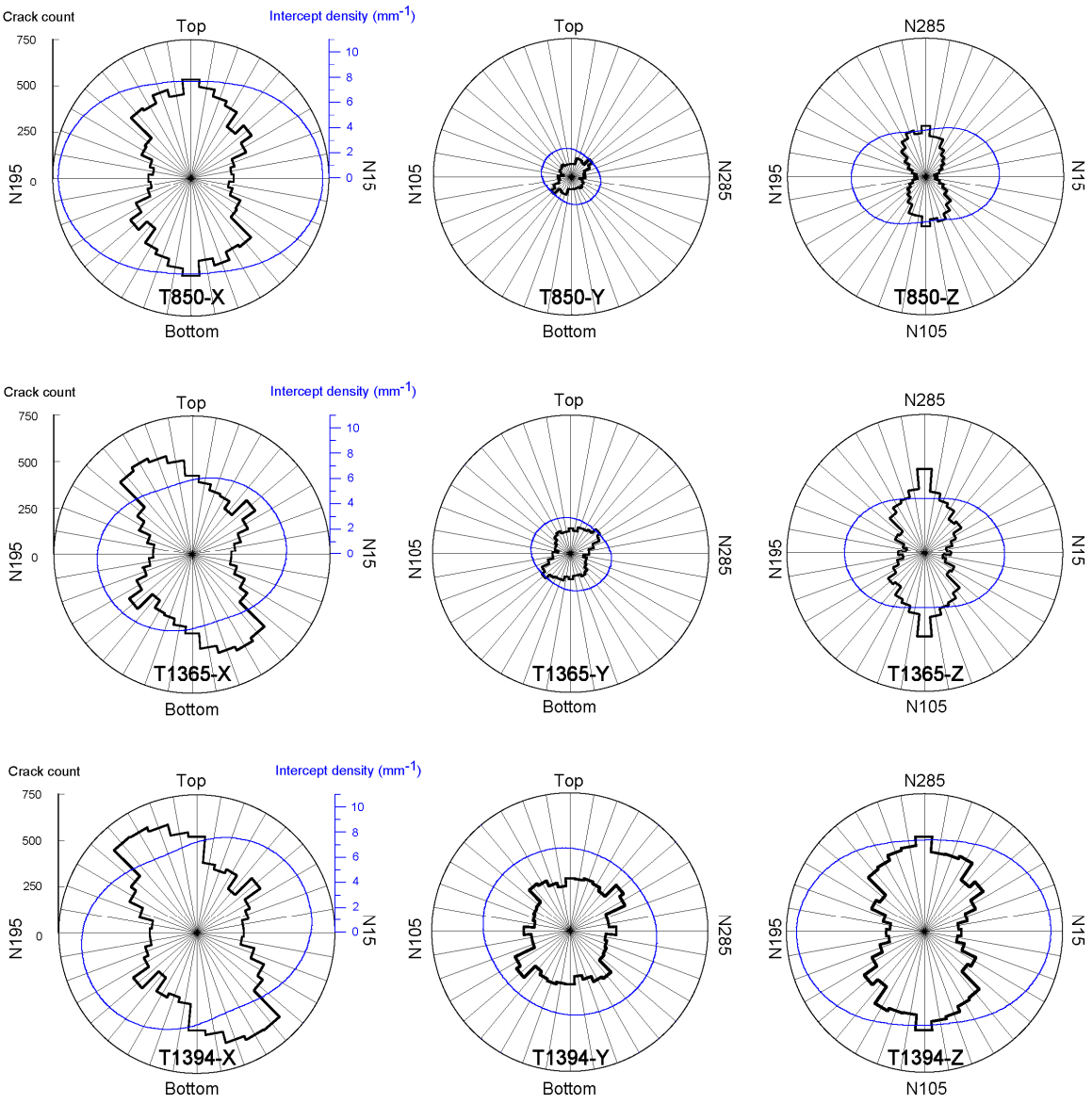

Figure 3.13 Polar plots of crack orientation and crack intercept density obtained from nine thin sections of three sandstones. The crack orientation is in black and the crack intercept density is in blue. The preferential orientations of microcracks gained from the intercept density are tabulated in Table 3.6.

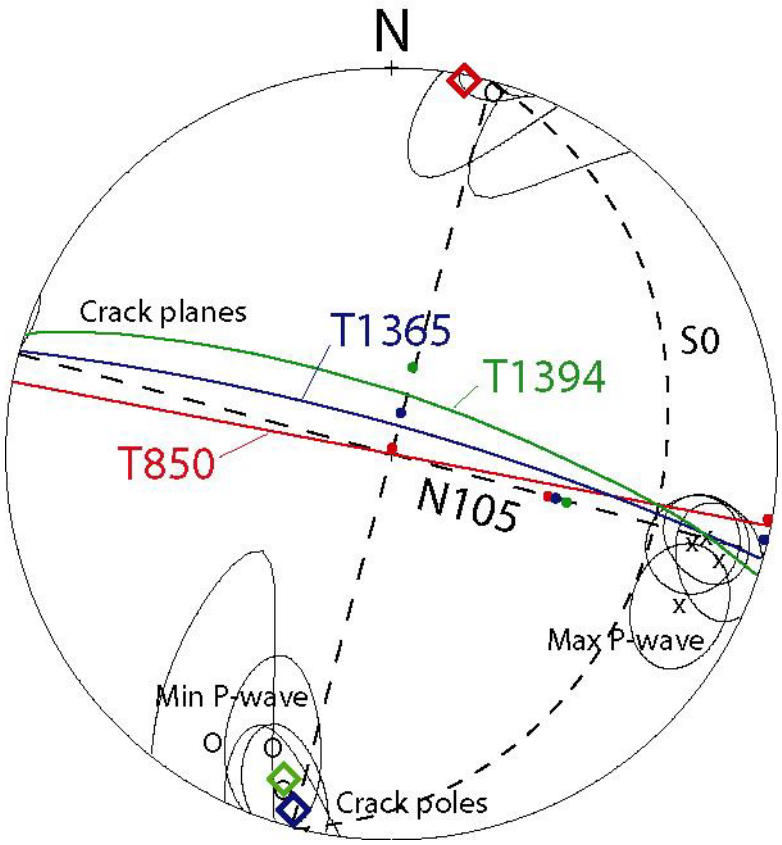

Figure 3.14 Comparison between the preferential crack planes in three sandstones and the P-wave data. The preferential crack planes in each sandstone are constrained by the anisotropic crack density data of the three orthogonal thin sections. The poles of the preferentially oriented crack planes fall in the proximity of the direction of the minimum P-wave velocity. The directions of the fast P-wave velocity are subparallel to the preferred orientations of the microcrack planes.

CHAPTER 4

CONCLUSION

1. The presence of water would weaken the TCDP country rock samples. Brittle strengths of the wet samples are lower than the dry ones by about 30% for samples that were cored along the same direction disregarding the petrographic facies.

2. The shaly siltstones have brittle strengths comparable to sandstones which have higher porosities, because large amount of clay minerals in the siltstones would make them mechanically weaker.

3. The results of mechanical strength, elastic modulus, and hydraulic permeability measurements reveal appreciable anisotropy, possibly induced by the bedding anisotropy in TCDP siltstones.

4. Microcracks in TCDP sandstones are preferentially oriented. The preferential crack planes are aligned with the azimuth N105°E with subvertical dipping angles and subparallel to the tectonic normal compression direction. The anisotropy of microcrack distribution provide constraints on the anisotropy of other physical properties such as elastic moduli, permeability and seismic wave velocity.

5. The measurements on TCDP siltstones suggest that thermal pressurization of pore fluid would be expected in these shaly rocks and may provide a mechanism for dynamic weakening of Chelungpu fault.

REFERENCES

Andrews, D.J. (2002), A fault constitutive relation accounting for thermal pressurization of pore fluid, *Journal of Geophysical Research*, **107**(B12), 2363, doi:10.1029/2002JB001942.

Angelier, J. (1986) Geodynamics of the Eurasia-Philippine Sea Plate boundary: Preface, *Tectonophysics*, **125**, IX-X.

Angelier, J., E. Barrier and H.T. Chu (1986), Plate collision and paleostress trajectories in a fold-thrust belt: The foothills of Taiwan, *Tectonophysics*, **125**, 161-178.

Baud, P., L. Louis, C. David, G.C. Rawling and T.-f. Wong (2005), Effects of bedding and foliation on mechanical anisotropy, damage evolution and failure mode, in *High-Strain Zones: Structure and Physical Properties* (eds. D. Bruhn and L. Burlini), Geological Society, London, **245**, 223-249.

Bernabe, Y. (1987), A wide range permeameter for use in rock physics, *International Journal of Rock Mechanics and Mining Sciences & Geomechanics Abstracts*, **24**(5), 309-315.

Boullier, A.-M., S.-R. Song, L.-W. Kuo and E.-C. Yeh (2007), Comparison of textures in the two TCDP gouges zones FZA1111 and FZB1136, *Abstract of the 2007 Taiwan Geosciences Assembly Meeting*

Brace, W.F., J.B. Walsh and W.T. Frango (1968), Permeability of granite under high pressure, *Journal of Geophysical Research*, **73**(6), 2225-2236.

Brace, W.F. (1980), Permeability of crystalline and argillaceous rocks, *International Journal of Rock Mechanics and Mining Sciences & Geomechanics Abstracts*, **17**, 241-251.

Brodsky, E.E. and H. Kanamori (2001), Elastohydrodynamic lubrication of faults, *Journal of Geophysical Research*, **106**(8), 16357-16374.

Caine, J.S., J.P. Evans, and C.B. Forster (1996), Fault zone architecture and permeability structure, *Geology*, **24**, 1025-1028.

Cardwell, R.K., D.S. Chinn, G..F. Moore and D.L. Turcotte (1978), Frictional heating on a fault zone with finite thickness, *The Geophysical Journal of the Royal Astronomical Society*, **52**, 525-530.

Chen, W.-S., K.-J. Lee, L.-S. Lee, D.J. Ponti, C. Prentice, Y.-G. Chen, H.-C. Chang, and Y.-H. Lee (2004), Paleoseismology of the Chelungpu fault during the past 1900 years, *Quaternary International*, **115-116**, 167-176.

Chester, F.M. and J.M. Logan (1986), Composite planar fabric of gouge from the Punchbowl fault, California, *Journal of Structural Geology*, **9**, 621-634.

David, C., T.-f. Wong, W. Zhu and J. Zhang (1994), Laboratory measurement of compaction-induced permeability change in porous rocks: Implications for the generation and maintenance of pore pressure excess in the crust, *Pure and Applied Geophysics*, **143**, 425-456.

Davis, D., J. Suppe and F.A. Dahlen (1983), Mechanics of fold-and-thrust belts and accretionary wedges, *Journal of Geophysical Research*, **88**, 1153-1172.

Donath, F.A. (1972), Effects of cohesion and granularity on deformational behaviour anisotropic rock. *Studies in Mineralogy and Precambrian Geology*, Geological Society of America Memoir, **135**, 95-128.

Evans, J.P., C.B. Forster and J.V. Goddard (1997), Permeability of fault-related rocks, and implications for hydraulic structure of fault zones, *Journal of Structural Geology*, **19**, 1393-1404.

Ho, C.S. (1988), *An Introduction to the Geology of Taiwan: Explanatory Text of the Geologic Map of Taiwan*, 2nd ed., Central Geological Survey, Taipei, Taiwan, 164pp.

Hung, J.-H., Y.-H. Wu, E.-C. Yeh, J.-C. Wu and TCDP Scientific Party (2007), Subsurface structure, physical properties, and fault zone characteristics in the scientific drill holes of Taiwan Chelungpu-fault Drilling Project, *Terrestrial Atmospheric and*

Oceanic Sciences, **18**(2), 271-293.

Ji, C., Helmberger, D.V., Song, T. A., Ma, K.-F. and Wald, D.J. (2001), Slip distribution and tectonic implication of the 1999 Chi-Chi, Taiwan, earthquake, *Geophysical Research Letters*, **28**(23), 4379-4382.

Ji, C., Helmberger, D.V., Wald, D.J. and Ma, K.-F. (2003), Slip history and dynamic implications of the 1999 Chi-Chi, Taiwan, earthquake, *Journal of Geophysical Research*, **108**(B9), 2412, doi:10.1029/2002JB001764.

Johnson, K.M. and P. Segall (2004), Imaging the ramp-décollement geometry of the Chelungpu fault using coseismic GPS displacements from the 1999 Chi-Chi, Taiwan earthquake, *Tectonophysics*, **378**, 123-139.

Kao, H. and W.-P. Chen (2000), The Chi-Chi earthquake sequence: Active, out-of-sequence thrust faulting in Taiwan, *Science*, **288**, 2346-2349.

Kuo, L.-W., S.-R. Song and H.-F. Chen (2005), Characteristics of clay mineralogy in the fault zone of the TCDP and its implication, *Eos Transactions AGU*, **86**(52), Fall Meeting Supplement, Abstract T43D-05.

Lachenbruch, A.H. (1980), Frictional heating, fluid pressure, and the resistance to fault motion, *Journal of Geophysical Research*, **85**, 6097-6112.

Lee, T.-C. and P.T. Delaney (1987), Frictional heating and pore pressure rise due to fault slip, *The Geophysical Journal of the Royal Astronomical Society*, **88**, 569-591.

Lo, T.-w., K.B. Coyner and M.N. Toksöz (1986), Experimental determination of elastic anisotropy of Berea sandstone, Chicopee shale and Chelmsford granite, *Geophysics*, **51**(1), 164-171

Lockner, D.A., C. Morrow, S.-R. Song, S. Tembe and T.-f. Wong (2005), Permeability of whole core samples of Chelungpu fault, Taiwan TCDP scientific drillhole, *Eos Transactions AGU*, **86**(52), Fall Meeting Supplement, Abstract T43D-04.

Louis, L., C. David, V. Metz, P. Robion, B. Menéndez and C. Kissel (2005),

Microstructural control on the anisotropy of elastic and transport properties in undeformed sandstones, *International Journal of Rock Mechanics and Mining Sciences*, **42**(7-8), 911-923.

Louis, L., T.-M. N. Chen, C. David, P. Robion, T.-f. Wong and S.-R. Song (2008), Anisotropy of magnetic susceptibility and P-wave velocity in core samples from the Taiwan Chelungpu-fault Drilling Project, *Journal of Structural Geology*, in press.

Ma, K.-F., E.E. Brodsky, J. Mori, C. Ji, T.-R. Song and H. Kanamori (2003), Evidence for fault lubrication during the 1999 Chi-Chi, Taiwan, earthquake (Mw7.6), *Geophysical Research Letters*, **30**(5), 1244, doi:10.1029/2002GL015380.

Mase, C.W. and L. Smith (1984), Pore-fluid pressures and frictional heating on a fault surface, *Pure and Applied Geophysics*, **122**(2-4), 583-607.

McKenzie, D. and J.N. Brune (1972), Melting on fault planes during large earthquake, *The Geophysical Journal of the Royal Astronomical Society*, **29**, 65-78.

Morrow, C.A. and D. Lockner (1994), Permeability differences between surface-derived and deep drillhole core samples, *Geophysical Research Letters*, **21**(19), 2151-2154.

Morrow, C., D. Lockner, S. Hickman, M. Rusanov and T. Röckel (1994), Effects of lithology and depth on the permeability of core samples from the Kola and KTB drill holes, *Journal of Geophysical Research*, **99**(B4), 7263-7274.

Nasseri, M.H., K.S. Rao and T. Ramamurthy (1997), Failure mechanism in schistose rocks, *International Journal of Rock Mechanics and Mining Sciences*, **34**, 460.

Niandou, H., J.F. Shao, J.P. Henry and D. Fourmaintraux (1997), Laboratory investigation of the mechanical behaviour of Tournemire shale, *International Journal of Rock Mechanics and Mining Sciences*, **34**, 3-16.

Otsuki, K., T. Uduki, N. Monzawa and H. Tanaka (2005), Clayey injection veins and pseudotachylyte from two boreholes penetrating the Chelungpu fault, Taiwan: Their implications for the contrastive seismic slip behaviors during the 1999 Chi-Chi earthquake, *The Island Arc*, **14**, 22-36.

Rice, J.R. (1992), Fault stress states, pore pressure distributions, and the weakness of the San Andreas Fault, in *Fault Mechanics and Transport Properties of Rocks* (eds. B. Evans and T.-f. Wong), Academic Press, 475-503.

Seront, B., T.-f. Wong, J.S. Caine, C.B. Forster, R.L. Bruhn and J. Fredrich (1998), Laboratory characterization of hydrothermal properties of a seismogenic normal fault system, *Journal of Structural Geology*, **20**, 865-881.

Shin, T.-C. and T.L. Teng (2001), An overview of the 1999 Chi-Chi, Taiwan, earthquake, *Bulletin of Seismological Society of America*, **91**(5), 895-913.

Sibson, R.H. (1973), Interactions between temperature and fluid pressure during earthquake faulting- A mechanism for partial or total stress relief, *Nature: Physical Science*, **243**, 66-68.

Sibson, R.H. (1977), Fault rocks and fault mechanisms, *Geological Society of London Journal*, **133**, 191-231.

Song, S.-R., L.-W. Kuo, E.-C. Yeh, C.-Y. Wang, J.-H. Hung and K.-F. Ma (2007), Characteristics of the lithology, fault-related rocks and fault zone structures in TCDP Hole-A, *Terrestrial Atmospheric and Oceanic Sciences*, **18**(2), 243-269.

Suppe, J. and J.H. Wittke (1977), Abnormal pore-fluid pressures in relation to stratigraphy and structure in the active fold-and-thrust belt of Northwestern Taiwan, *Petroleum Geology of Taiwan*, **14**, 11-24.

Teng, L.S. (1987), Stratigraphic records of the late Cenozoic Penglai orogeny of Taiwan, *Acta Geologica Taiwanica*, **25**, 205-224.

Teng, L.S. (1990), Geotectonic evolution of Late Cenozoic arc- continent collision in Taiwan, *Tectonophysics*, **183**, 57-76.

Teng, L.S. (1996), Extensional collapse of the northern Taiwan mountain belt, *Geology*, **24**, 945-952.

Vernik, L., D. Lockner and M.D. Zoback (1992), Anisotropic strength of some typical

metamorphic rocks from the KTB pilot hole, Germany, *Science of Drilling*, **3**, 161-169.

Jeen-Hwa Wang (2006), Energy release and heat generation during the 1999 M_s7.6 Chi-Chi, Taiwan, earthquake, *Journal of Geophysical Research*, **111**, B11312, doi:10.1029/2005JB004018.

Wu, H.-Y., K.-F. Ma, M. Zoback, N. Boness, H. Ito, J.-H. Hung and S. Hickman (2007), Stress orientations of Taiwan Chelungpu-Fault Drilling Project (TCDP) hole-A as observed from geophysical logs, *Geophysical Research Letters*, **34**(1), doi:10.1029/2006GL028050.

Yang, T.F., Walia V., Lee H.-F., S.-R. Song and C.-Y. Wang (2005), Compositions of on-site monitoring on dissolved gas of drilling mud flow and pore-gases of drilled cores of TCDP, *Eos Transactions AGU*, **86**(52), Fall Meeting Supplement, Abstract T51A-1315.

Yeh, E.-C., H. Sone, T. Nakaya, K.-H. Ian, S.-R. Song, H.-J. Hung, W. Lin, T. Hirono, C.-Y. Wang, K.-F. Ma, W. Soh and M. Kinoshita (2007), Core description and characteristics of fault zones from Hole-A of the Taiwan Chelungpu-fault Drilling Project, *Terrestrial Atmospheric and Oceanic Sciences*, **18**(2), 327-357.

Yue, L.-F., J. Suppe and J.-H. Hung (2005), Structural geology of a classic thrust belt earthquake: the 1999 Chi-Chi earthquake Taiwan (M_w=7.6), *Journal of Structural Geology*, **27**, 2058-2083.

Zhu, W. and T.-f. Wong (1997), The transition from brittle faulting to cataclastic flow: Permeability evolution, *Journal of Geophysical Research*, **102**(B2), 3027-3041.